



Full length article

Simulation of crystal plasticity in irradiated metals: A case study on Zircaloy-4

Chris Hardie^{a,c,*}, Rhys Thomas^b, Yang Liu^c, Philipp Frankel^b, Fionn Dunne^c^a UK Atomic Energy Authority, Culham Centre for Fusion Energy, Oxfordshire, UK^b University of Manchester, Oxford Road, Manchester, UK^c Imperial College London, South Kensington Campus, London, UK

ARTICLE INFO

Article history:

Received 15 July 2022

Revised 7 September 2022

Accepted 11 September 2022

Available online 14 September 2022

Keywords:

Crystal plasticity

Irradiation

Zirconium alloys

Localization

Dislocation theory

ABSTRACT

A classical crystal plasticity formulation based on dislocation slip was extended to include the mechanisms of dislocation channelling, with associated strain softening which is observed in many alloys post irradiation. The performance of the model was evaluated against experimental data on Zircaloy-4, which included engineering stress-strain response and high-resolution digital image correlation strain mapping. Variants of the model were developed to evaluate the influence on the strain hardening law used, comparing hardening based on a linear relationship for effective plastic strain with that based on the evolution of geometrically necessary dislocations. In addition, governing equations for simulating the interaction between gliding dislocations with various types of irradiation defect were investigated; this included the comparison of isotropic and anisotropic interactions based on the resultant reaction segments for each interaction. It was shown that the engineering stress-strain response measured by experiment could be captured by many of the model variants, but the simulation of characteristic strain heterogeneity was more sensitive to the model used. Direct modelling of the HRDIC experiments indicated that the model successfully predicted the activation of slip systems in many cases and exhibited localised strain distribution as observed in the experiment. In all models localised kink band formation was predicted, which is not observed experimentally, which highlights limitations in modelling of softening materials with a local crystal plasticity approach and a required area of development going forward.

Crown Copyright © 2022 Published by Elsevier Ltd on behalf of Acta Materialia Inc.

This is an open access article under the CC BY license (<http://creativecommons.org/licenses/by/4.0/>)

1. Introduction

The structural integrity of next generation nuclear reactors will need to be assessed in the absence of full and complete experimental data, therefore simulation techniques are required to provide a means of greater understanding and prediction. The crystal plasticity finite element method (CPFEM) is a strong candidate to support this requirement because the predominant effect of irradiation damage on the deformation processes, and the subsequent failure of a material, occur at the crystalline scale. As demonstrated in [1], simulation of plasticity at this scale can be based on a mechanistic understanding of dislocation slip; this can capture the interdependent relationships that govern plasticity over a highly multidimensional parameter space, including temperature, strain rate and loading history. The development of mechanistically informed crystal plasticity models has the potential to enhance un-

derstanding of material behaviour in nuclear environments; to inform alloy development beyond empirical trial and error; and critically to provide a predictive tool that can be used for structural integrity assessment of components operating in uncharted conditions of next generation nuclear reactors.

Practically all commercial structural alloys exhibit hardening and embrittlement at the high neutron doses anticipated for next generation fission and fusion reactors. After doses of just 0.1 displacements per atom (dpa), many alloys exhibit strain localisation, resulting in prompt necking at yield [2,3]. Nuclear cladding alloy Zircaloy-4 is a good example of this behaviour and exhibits highly anisotropic mechanical behaviour due to its hexagonal close packed (HCP) structure. Increases in yield stress and ultimate tensile stress [4–8] and indentation hardness [9] have been measured for pure Zr and its alloys. A clear yield point is observed after irradiation, which becomes more prominent with increasing test temperatures and strain rates in pure Zr [10]. The extent of hardening appears to be independent of texture/loading direction [9,11] and dislocation slip occurs in localised bands, attributed to dislocation channelling [4,11–15]. A reduction in work hardening and remark-

* Corresponding author at: UK Atomic Energy Authority, Culham Centre for Fusion Energy, Oxfordshire, UK.

E-mail address: Chris.Hardie@ukaea.uk (C. Hardie).

able loss of ductility is observed after irradiation to low doses (e.g. 0.01 dpa), with immediate necking and strain softening promoted at elevated test temperatures [4,7,11,12].

Dislocation channelling occurs due to local removal of irradiation induced defects by interaction with glissile dislocations, which creates a preferred pathway for dislocation glide between regions of dense defect populations [16]. Several possible reactions between glissile dislocations and defects exist, including bypassing, shearing or transforming, partial or full absorption, temporary absorption, and dragging or sweeping of the defect [17]. Owing to the typical irradiation damage microstructures of zirconium alloys as observed by transmission electron microscopy (TEM) [18], much of the modelling work that investigates dislocation-defect interactions in zirconium focuses on dislocation loop defects (hereafter referred to as ‘loops’). Molecular dynamics (MD) simulations have shown that the reaction with loops depends on the type of glissile dislocation (edge, mixed or screw) and its Burgers vector compared to that of the loop [19,20]. Unfortunately all MD studies to date have only focused on dislocation-loop interactions associated with prismatic slip, however a different likelihood of annihilation reactions for both prismatic and basal slip have been predicted by dislocation dynamics (DD) [21]. Differences between the likelihood of loop annihilation have been used to explain the observed transition of preferred slip system from prismatic to the basal system in Zircaloy-4 after irradiation [8,14].

Despite the importance of Zr alloys in the nuclear industry, the development of representative models that simulate its mechanical behaviour has received little attention. The striking effects irradiation has on the anisotropic plastic deformation of Zr provides considerable challenges to the capability of CPFEM to capture physically representative plasticity mechanisms in irradiated alloys. Notably, the strong localisation of slip into discrete bands differentiates the nature of intragranular deformation in the irradiated state compared to the much more diffuse slip observed in unirradiated Zircaloy-4. Experimental observations and measurements of slip using high-resolution digital image correlation (DIC) in this alloy were reported in [15] in which the extraordinary differences between unirradiated and proton-irradiated slip characteristics are made very apparent, even for relatively low irradiation doses. This is important because of the irrevocable link between highly localised slip, dislocation pile-up (eg at a grain boundary or hydride in the context of Zircaloy-4 application), stress concentration and the resulting onset of crack nucleation through slip-driven fatigue [22] or delayed hydride cracking [23,24]. Recent work in the quantitative characterisation of irradiation-induced discrete and localised slip in tensile loaded samples [15] provides a rich source of data with which to establish and test new crystal plasticity modelling formulations which capture mechanistically the observed slip localisation effects.

Hence in this paper, the development of a mechanistically informed CPFEM framework is firstly presented which captures the effects of irradiation on Zircaloy-4. This includes both initial hardening by loop density increase and subsequent channel clearing and softening, leading to highly discrete slip band formation, and resulting material softening. High-resolution DIC observations of irradiated and unirradiated Zircaloy-4 described in [15] provide detailed mapping of slip activation and straining both intra- and transgranularly on free surfaces of samples subjected to well-defined tensile, strain-controlled loading. This facilitates detailed assessment of crystal plasticity model predictions for both unirradiated and irradiated conditions against experimental measurements of slip activation. In what follows, the CPFEM model is introduced and the mechanistic approach to capture irradiation effects described. This is assessed firstly at the ‘coarse strain’ level for which computed macro-level average stress-strain behaviour

for differing irradiation doses is considered against independent data in the literature. Secondly, the micro-strain level is analysed in which explicit model representations of characterised and tested microstructures are presented. Detailed evaluations were carried out on FE model parameters and boundary conditions, as well as the resulting predicted slip activations and strain maps, against the experimental observations.

2. Crystal plasticity finite element method irradiation model development

A well-established crystal slip rule for HCP Zr is utilised here which is dislocation based and has been developed to allow for lattice curvature and geometrically necessary dislocation effects, as reported in the literature [25,26]. This is appropriate for the current study of irradiation effects since at the crystalline scale, the manifestation of irradiation occurs as dislocation slip strengthening with concurrent, for appropriate slip systems, channel clearing, and dislocation slip softening. The dislocation-based slip rule provides an effective means to represent the mechanistic effects of irradiation in CPFEM as a function of the irradiation induced defect microstructure. The slip rule defines the shear strain rate for each of the 30 HCP slip systems activated (denoted by superscript $k = 1, \dots, 30$) and is based on the occurrence of both thermal and athermal events, the former corresponding to thermally activated escape of pinned dislocations (giving rise to a rate sensitivity) and the latter to dislocation glide and hardening (either through multiplication of statistically stored dislocations, lattice curvature and GNDs, or irradiation hardening) and irradiation-induced strain softening. It is given by [1]:

$$\dot{\gamma}^k = \rho_m v_g b^k = \rho_m v b^{k^2} \exp\left(-\frac{\Delta F}{kT}\right) \sinh\left(\frac{(|\tau^k| - \tau_c^k) \Delta V}{kT}\right) \text{sgn}(\tau^k) \quad (1)$$

where ρ_m , b^k and v_g are the mobile dislocation density, Burgers vector and average dislocation velocity respectively, v is the attempt frequency for dislocation jumps (i.e. unpinning opportunities), ΔF is the activation energy and ΔV is the activation volume associated with thermally activated dislocation unpinning. τ^k is the resolved shear stress on slip system k and τ_c^k represents the athermal component of slip resistance, with ΔV and ΔF controlling the thermal component. Given the limited availability of data for irradiated Zircaloy-4, only τ_c^k is taken to be dependent on irradiation condition, because of the better understanding associated with irradiation effects on hardening and softening. Thus both ΔV and ΔF , which control crystal slip system rate sensitivity, are taken to remain independent of irradiation, but of course quantitative knowledge as it becomes available can be incorporated. The unirradiated Zircaloy-4 parameters for this model have been previously determined from DIC-measured intragranular slip measurements [25], consistent with microcantilever single crystal testing [27]. The parameters used throughout this work are given in Table 1 [25]. These material properties have been carefully validated against high resolution digital image correlation (HRDIC) of intra- and trans-granular creep strains experiments on polycrystalline samples, as well as isolated measurement of individual slip system types by micro-mechanical testing [27].

The inclusion of irradiation effects requires two primary effects to be addressed which are irradiation hardening manifested by increased yield stress and indentation hardness, and post irradiation strain softening, resulting in a decrease in flow stress with increasing strain and strain localisation. These are addressed in Sections 2.1 and 2.1, respectively.

Table 1
Elasto-plastic material properties of unirradiated Zircaloy-4 at 20 °C [25].

	Parameter	Unit	Value	
ELASTIC	E_x	MPa	98 308	
	E_y	MPa	132 208	
	G_{xz}	MPa	32 010	
	ν_{xy}		0.4006	
	ν_{xz}		0.2375	
PLASTIC	ρ_m	μm^{-2}	0.01	
	ν	Hz	10^{11}	
	b <a> slip	μm	3.2×10^{-4}	
	b <a+c> slip	μm	6.0×10^{-4}	
	k	pJ/K	1.381×10^{-11}	
	ΔV	b^3	20.93	
	ΔF	pJ	5.127×10^{-8}	
	basal (a) ($k = 1$ to 3)	τ_c^{ba}	MPa	204.0
	prismatic (a) ($k = 4$ to 6)	τ_c^{pr}	MPa	153.0
	pyramidal (a) ($k = 7$ to 12)	τ_c^{py}	MPa	153.0
	pyramidal (a + c) 1^{st} ($k = 13$ to 24)	τ_c^{py1}	MPa	532.4
	pyramidal (a + c) 2^{nd} ($k = 25$ to 30)	τ_c^{py2}	MPa	2662.1

2.1. Irradiation hardening

Irradiation introduces multiple types of defect to the lattice, which in addition to pre-existing microstructural constituents and lattice friction (Peierls barrier), resist dislocation glide and increase slip system strength by mechanisms universally referred to as irradiation hardening. The most relevant and commonly used model for the treatment of irradiation induced defects is the Taylor equation [28–33]:

$$\Delta\tau = \alpha Gb\sqrt{\rho} \quad (2)$$

where $\Delta\tau$ is the component of the τ_c^k attributed to an array of discrete obstacles, α is the obstacle strength with a value ranging from 0 (ineffectual) to 1 (impenetrable), G is the shear modulus of the material and ρ is the area density of obstacles. For discrete obstacles $\rho = Nd$ is used, where N is the volumetric number density and d is the average diameter.

The multiple constituents that provide strength can be treated using 'superposition laws', which have been the subject of discussion since the early development of plasticity theory [34]. Surprisingly, a consensus on superposition of the various hardening components is yet to be achieved, evident by a variety of fundamentally different formulations featured in recent literature. The two common categories of superposition laws that feature in CPFEM studies of irradiated materials are linear superposition, $\tau_c = \tau_1 + \tau_2 + \dots$ [31–33,35,36], and square superposition, $\tau_c^2 = \tau_1^2 + \tau_2^2 + \dots$ [28–30]. Despite wide use of linear superposition, there are strong arguments that a square superposition law is most appropriate for dispersed obstacles such as irradiation induced defects. The theoretical argument is best given by Kocks [34], which considers the distribution of two types of obstacle in the lattice that have an identical resistance to dislocation glide. In this model there is no difference between the two defect types and their densities can simply be summed, leading to the square superposition of both types of obstacles. This theory is strengthened by considering the many experimental observations that irradiation hardening reduces as the unirradiated strength of the alloy increases. This is directly reported for Zirconium alloy [7] and suggests that the hardening contribution from irradiation-induced defects is less influential when competing with other hardening mechanisms.

Inspired by Kocks [34], a mixed superposition approach was developed for this work, where components of lattice friction are summed linearly with the total contribution from discrete obsta-

cles summed by square superposition:

$$\tau_c^k = (1 - X)\tau_0^k + Gb^k \sqrt{\left(\frac{X\tau_0^k}{Gb^k}\right)^2 + \alpha^2\rho_\varepsilon + P_l k^2} \quad (3)$$

The unirradiated slip strength (CRSS), τ_0 , is split in two parts by the parameter X , where the component of strength associated with discrete obstacles is $X\tau_0$ and the lattice friction component of strength is $(1 - X)\tau_0$. Strain hardening is represented by a dislocation density multiplied by an obstacle strength, α^2 . Two forms of dislocation density evolution are compared. The first, based on evolution of statistically stored dislocations, comprises a linear relationship with effect effective plastic strain:

$$\rho_\varepsilon = Y\bar{\varepsilon}_p \quad (4)$$

using a hardening coefficient Y (m^{-2}). The second is based on hardening which results from geometrically necessary dislocations (GNDs) which support lattice curvature obtained from the curl of the plastic deformation gradient, \mathbf{F}_p [1,35]:

$$\mathbf{A}\rho_{\text{GND}} = \nabla \times \mathbf{F}_p \quad (5)$$

where \mathbf{A} is a matrix with columns formed of reshaped tensor products $\mathbf{l}^j \otimes \mathbf{b}^k$, with dislocation line direction \mathbf{l}^j and j representing all 30 edge and 9 screw dislocation types. The GND density for each dislocation type j is approximated by minimisation of dislocation line energy by finding the L^2 norm [37]. The total dislocation density is calculated as the sum of all densities:

$$\rho_\varepsilon = \sum_{j=1}^N |\rho_{\text{GND}}^j| \quad (6)$$

Finally, the component of strength due to irradiation is given by:

$$P_l k^2 = \sum_{i=1}^{N_{\text{loop}}} H_i^{k^2} N_i d_i \quad (7)$$

where H_i^k is a matrix of coefficients describing the obstacle strengths for different types of defect (denoted with subscript i) with density, N , and average diameter, d , acting on each slip system, k . The components of H_i^k provide the required degree of freedom in the model to simulate the anisotropy between different dislocation-defect reactions as described in Section 2.3.

2.2. Strain softening

Given that dislocation channelling occurs due to the localised removal of defects and softening by dislocation plasticity, τ_c^k should evolve locally with strain. Previous studies have demonstrated various approaches which fall into three categories.

The first category updates the defect density with a linear relationship to the plastic shear strain [28–31,33]; this has the general form:

$$\dot{N} = \varphi \frac{Nd}{b} |\dot{\gamma}| \quad (8)$$

where φ represents the probability of defect annihilation and is used to scale the rate of annihilation relative to the shear rate. Examples of defect annihilation functions in this category vary in complexity, including defect densities and annihilation specific to individual slip systems, terms that take mobile dislocation density into account, and even the difference between screw and edge dislocation densities.

The second category includes examples of non-linear functions including the use of linear functions between specified strain ranges [35] and an exponential function [38], applied to the total shear strain (γ) as shown in Eq. (9) and Eq. (10) respectively.

$$f(\gamma^k) = \begin{cases} 0 & \gamma \leq \gamma^{crit} \\ -\frac{\gamma - \gamma^{crit}}{\gamma^{sat} - \gamma^{crit}} & \gamma > \gamma^{crit} \end{cases} \quad (9)$$

$$f(\gamma) = e^{-\left(\frac{\gamma}{\bar{\gamma}}\right)} \quad (10)$$

In the above equations the fitting parameters are γ^{crit} and γ^{sat} which define the range of shear strain (lower and upper limits) where softening takes place and φ is a softening rate. Here the hardening component associated with irradiation is explicitly calculated and underlying defects are not considered.

The final category focuses on loop defects and accounts for the geometric relationship between the loop and gliding dislocation [32,39,40]. Here a ‘damage descriptor tensor’ describing the defect microstructure is defined as:

$$\mathbf{H} = 1/V \sum_i 3d_i^i (\mathbf{I} - \mathbf{n}_i^i \otimes \mathbf{n}_i^i) \quad (11)$$

where d_i is the loop diameter, \mathbf{n}_i is the normal of the loop habit plane and V is the volume of the simulation cell. Here, index i represents each loop within the simulation cell. The slip system geometry is defined by its normal, \mathbf{n}^k with:

$$\mathbf{Q}^k = \mathbf{n}^k \otimes \mathbf{n}^k \quad (12)$$

The slip system specific hardening component associated with discrete irradiation defects is represented by $\mathbf{Q}^k : \mathbf{H}$.

Evolution of the damage descriptor tensor is defined as:

$$\dot{\mathbf{H}} = -\eta \sum_{\alpha} (\mathbf{Q}^k : \mathbf{H}) \mathbf{Q}^k |\dot{\gamma}^k| \quad (13)$$

Here η is a scaling factor to set the rate of change. The tensor double dot product $\mathbf{Q}^k : \mathbf{H}$ simply results in the loop density scaled by the contact density based on the perpendicularity of the loop and the slip plane. This suggests that loops do not interact with dislocations on slip planes with a normal that is parallel with the loop habit plane. As demonstrated by the MD simulations of Bacon et al. [17], dislocation-loop interactions are complex with reactions resulting in new segments and junctions. Thus, despite the mathematical elegance of this technique there is little physical basis that supports the linear scaling with contact density.

To maintain an approach that is based on a single, consistent mechanistic description of plasticity, the mathematical description of dislocation-loop annihilation reactions can be fully correlated with the same mechanisms used to define the slip law

given in Eq. (1). The slip plane area traversed by the unpinning of a dislocation can be approximated by $A = l\bar{x}$, where l is the defect spacing. Approximating that the average glide distance (\bar{x}) is equal to the defect spacing ($\bar{x} \approx l \approx \frac{1}{\sqrt{N_i d_i}}$) for a regular array of defects, the slip plane area traversed by the unpinning of a dislocation is:

$$A \approx \bar{x}l \approx \frac{1}{N_i d_i} \quad (14)$$

The rate of dislocation-defect reactions occurs at the rate of unpinning from the defect for each dislocation, Γ^k . The average dislocation glide velocity introduced in Eq. (1) is equal to the average glide distance, \bar{x} , multiplied by the rate of unpinning:

$$v_g = \bar{x} \times \Gamma^k = \frac{A}{l} \Gamma^k = \frac{1}{N_i d_i l} \Gamma^k \quad (15)$$

By inserting this expression into Eq. (1) the strain rate on slip system k is given by:

$$\dot{\gamma}^k = \rho_m v_g b^k = \frac{\rho_m b^k A}{l} \Gamma^k = \frac{\rho_m b^k}{N_i d_i l} \Gamma^k \quad (16)$$

Rearranging for the unpinning (reaction) rate for all gliding dislocations and defects gives:

$$\Gamma^k \rho_m = \frac{\dot{\gamma}^k l}{b^k A} = \frac{\dot{\gamma}^k \sqrt{N_i d_i}}{b^k} \quad (17)$$

Therefore, the loop density is evolved explicitly as a function of strain on all slip systems for each time increment, Δt , and loop type, i , by¹:

$$N_{it+\Delta t} d_i = N_{it} d_i - \sum_{k=1}^{N_{sys}} \psi^k_i \frac{|\dot{\gamma}_t^k| \sqrt{N_{it} d_i}}{b^k} \Delta t \quad (18)$$

Here ψ^k_i includes 30×3 coefficients which incorporate the probability of each reaction resulting in loop annihilation, which accounts for the various interactions of all slip systems and Burgers vector combinations. Simulations and experiments have indicated that the reaction between loops and gliding dislocations is dependent on both temperature and strain rate [41,42], however given the absence of experimental data which covers these parameters for zirconium alloys, ψ^k_i in this work is defined by constants.

2.3. Anisotropic dislocation-defect interaction

It has been shown by atomistic simulations [19–21] and indicated by experiment [8,14] that the reaction between gliding dislocations and dislocation loops is different for different slip systems and loop Burgers vectors. It was suggested that the loop annihilation/clearing is more likely if the Burgers vector of the reaction segment between the glisile dislocation and the loop remained in the slip plane, $\mathbf{r}^k_i = \mathbf{b}^k + \mathbf{b}^i$, which can be established with the following dot product:

$$\mathbf{n}^k \cdot \mathbf{r}^k_i = a^k_i \quad (19)$$

where \mathbf{n}^k is the slip plane normal and the superscripts k and i represent the slip plane and loop respectively. The reaction segment is in the slip plane when $a^k_i = 0$. For slip on the basal, prismatic and pyramidal systems, which are most active during deformation along the rolling direction as studied in this work, the above is equivalent to when the Burgers vectors of the gliding dislocation and loop are equal.

¹ Indices i , k and t in Eq. (14) to Eq. (19) refer to defect type, slip system and time respectively, thus these indices do not follow index notation.

Table 2
Conditions selected with damage microstructure for calibration of the CPFEM model.

Condition	Loop Density ($10^4 \mu\text{m}^{-3}$)	N_i ($10^4 \mu\text{m}^{-3}$)	Loop Diameter (nm)	Yield Stress (MPa)
Unirradiated	0	0	N/A	383
0.001 dpa	1.1	0.367	1.2	438
0.8 dpa	6.1	2.033	1.4	598

TEM observations have shown that irradiation results in a population of several types of defects in Zirconium, from single and small clusters of interstitials and vacancies, to dislocation loops with both $\langle a \rangle$ and $\langle c \rangle$ type burgers vectors [18]. Larger defects that are observable in the TEM are assumed to be the dominant component of irradiation hardening in this study, thus only the population of dislocation loops are considered. For the low irradiation doses studied here dislocation loops may have Burgers vectors in the three $\langle a \rangle$ axes ($[2\bar{1}10]$, $[2\bar{1}\bar{1}0]$ and $[2\bar{1}10]$), thus the total dislocation loop density measured by TEM was equally distributed into three groups (denoted by index i), i.e. $N_i = \frac{N_{total}}{3}$ for $i = 1, 2, 3$.

The crystal slip rule developed above to incorporate irradiation hardening, followed by channel clearing and softening in appropriate activated slip systems, is implemented within a standard crystal plasticity user material subroutine (UMAT) for Abaqus FEA software, originally developed and described in [1]. This included an implicit formulation using a Newton-Raphson method to solve for the interdependent relationship between the fraction of elastic and plastic deformation, and the stress for each integration point for each increment in time within the finite element model. For all simulations presented here, twenty-noded quadratic hexahedral, reduced integration elements (C3D20R) were used.

A number of analyses are carried out in what follows using differing forms of the crystal plasticity formulation in order to provide comparisons of results with respect to representation of the stress-strain response (Section 3) and strain distributions (Section 4) of un-irradiated and irradiated Zircaloy-4. For clarity, these are described by the following acronyms:

ISO-LH – ISOTropic dislocation-defect interaction (H^k_i and ψ^k_i defined by a single constant) and Linear strain Hardening (Eq. (4)) and no GND hardening

ANI-LH – ANISotropic dislocation-defect interaction and Linear strain Hardening (Eq. (4)) and no GND hardening

ANI-GND – ANISotropic dislocation-defect interaction and strain hardening based on GND density only (Eqs. (5) & (6))

3. Stress-strain parameterisation

In this section, the CPFEM model presented above is utilised to investigate the macroscopic stress-strain response of Zircaloy-4 subject to differing irradiation doses and compared with independent data in the literature. Hence polycrystal simulations are carried out which reproduce the experimental sample texture and uniaxial strain-controlled loading.

The comprehensive study by Farrell et al. [2] was selected to assess the CPFEM model because it included both stress-strain response of Zircaloy-4 as a function of irradiation dose and the corresponding TEM data about the irradiation microstructure (shown in Table 2).

The alloy used was annealed at 670°C for 30 min in vacuum, which produced a recrystallised microstructure of equiaxed grains with a mean grain diameter of 13 μm . The tensile specimens used for these tests were machined in the rolling direction (RD) and

testing was conducted at a strain rate of 10^{-3} s^{-1} . Irradiation was conducted in High Flux Isotope Reactor at a temperature $< 100 \text{ }^\circ\text{C}$.

For the polycrystal model, a representative volume element (RVE) with 201 grains was constructed based on an as-received zircaloy-4 material with a typical rolling texture (c -axes along TD direction), and uniaxial loading was specified along the axis corresponding to the RD. Experimental (EBSD) data from rolled Zircaloy-4 were extracted using MATLAB/MTEX-5.1.1 package, this including grain orientation/misorientation distribution, grain size and grain shape distribution [25]. The geometric and crystallographic information were imported into the NEPER software package [43] to generate the polycrystalline RVE model. This model was scaled in size to give the mean grain diameters of 13 μm to match that reported from the experiment [2]. A previous convergence study has shown that the number of grains must be greater than ~ 150 to achieve convergence of the local and global mechanical response [44], which is satisfied here. A structured mesh with 1 μm elements was used, which has been validated through a previous convergence study [25].

The cube bottom surface (normal to loading) was fixed in the loading direction, and a selected node on the same surface was fixed to prevent rigid body movement. Displacement was applied on the opposite (top) surface to introduce tensile loading. This allowed Poisson contraction in the directions perpendicular to loading. The cube edge length was 45.5 μm , and a total displacement of 4.55 μm was applied to the loaded surface linearly over 100 s to match the experimental strain rate.

The slip rule incorporating irradiation induced hardening and softening given in Eqs. (1) to (19) contains several material parameters, giving the potential for non-unique solutions. However, given the distinct mechanistic definitions of the parameters it was possible to carry out fitting to the experiment using a systematic approach, which largely isolated single parameters to features of the stress-strain response. The only exception was the interdependency between X (the fraction of strength attributed to discrete obstacles) and the annihilation probability, ψ which both influence the rate of softening. In the absence of experimental data exploring variation in pre-existing discrete obstacle densities, a value for X was found by solving the simultaneous equations (using Eq. (3)) produced using measured yield stresses for the three conditions outlined in Table 2, such that for each case:

$$r = \tau_{c_exp} - \tau_{c_model} = \tau_{c_exp} - \left[(1 - X)\tau_c^{pr} + Gb \sqrt{\left(\frac{X\tau_c^{pr}}{Gb}\right)^2 + H^2ND} \right] = 0 \quad (20)$$

The CRSS for prismatic slip was used in this method, given this is the dominant slip system for deformation in the rolling direction. An iterative solution returned $X = 0.31$ and $H = 1.24$; this suggests that approximately 31% of the strength of Zircaloy-4 is due to discrete obstacles such as secondary phase precipitates (SPPs) in the microstructure. Annealed pure Zirconium has a yield stress of 230 MPa [45], which is 60% of that for Zircaloy-4, thus a value of $X = 0.31$ is plausible given that the increase in the alloy is

Table 3
Model parameters found by fitting the model to strain-strain curves of Zircaloy-4 in the unirradiated and irradiated (0.8 dpa) condition.

Model	Parameter	Unit	Value
All	τ_c^{ba}	MPa	187.7
	τ_c^{pr}	MPa	140.8
	τ_c^{py}	MPa	140.8
	τ_c^{py1}	MPa	489.8
	τ_c^{py2}	MPa	2449.1
LH	$\alpha^2 Y$	$\mu.m^{-2}$	130
GND	α^2		0.05
ISO	H		1.4
ANI	ψ		0.01
	$H_i^k (a_i^k = 0)$		1.25
	$H_i^k (a_i^k > 0)$		1.875
	$\psi_i^k (a_i^k = 0)$		0.50
	$\psi_i^k (a_i^k > 0)$		0.00

likely due to a mixture of solid solution strengthening and discrete secondary phase precipitates.

Maintaining a value of $X = 0.31$, the LH and GND models were parameterised by fitting τ_c , α^2 and Y , using the unirradiated stress-strain curve and the ISO and ANI models were parameterised by fitting H , H_i^k and ψ_i^k using the stress-strain curve of the alloy irradiated to 0.8 dpa. This approach isolated the fitting of each parameter independently to ensure a unique result. The model parameters and results are shown in Table 3. A parameter sensitiv-

ity study for a single slip system is presented in Appendix B. This demonstrates the relatively small influence parameter X and the linear strain hardening coefficient $Y\alpha^2$ has on the model behaviour representing the influence of irradiation.

Following this, the parameters were held fixed, and the CPFEM model run again for the lower dose (0.001 dpa) condition with lower loop density and average diameter. The comparison between the simulation and the experimental data is shown in Fig. 1.

The stress-strain response for the unirradiated case follows the general trend relatively well, with little difference in the hardening behaviour. For the material irradiated to 0.8 dpa, the increase in yield stress and overall softening with strain is captured well. The initial yield drop which has been observed in several studies (e.g. see [4,11]) is not reproduced by the ISO-LH model, but is reproduced with the anisotropic dislocation-defect interaction models (ANI-LH and ANI-GND). (Note that the strong strain softening observed at a strain of about 9% is not due to irradiation directly but sample necking and failure.) The elastic-plastic transition and yield point is represented relatively accurately for the 0.001 dpa case, however the degree of strain softening is overpredicted by the simulation.

The total plastic strain distribution plotted on the surfaces of the textured polycrystal model for all three simulations using the ISO-LH model is shown in Fig. 2. The plastic strain distribution is heterogeneous in all three conditions due to elastic anisotropy between each grain with respective orientations. There is negligible

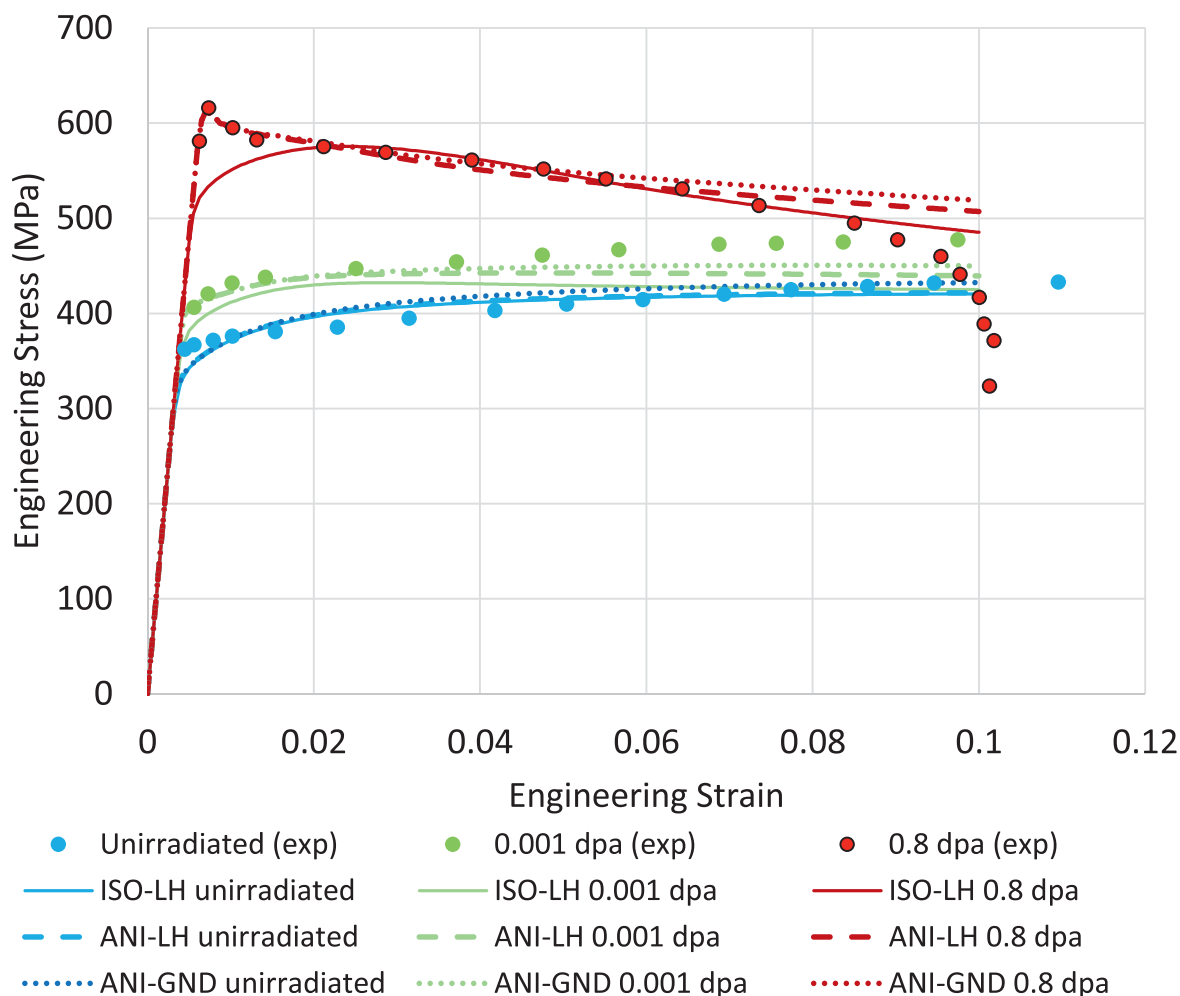
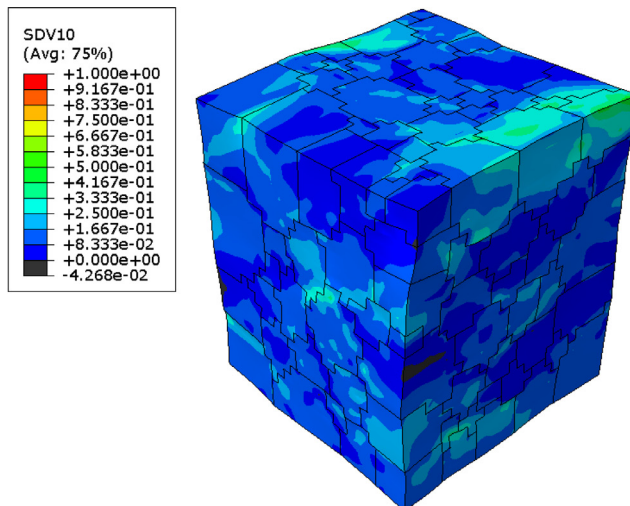
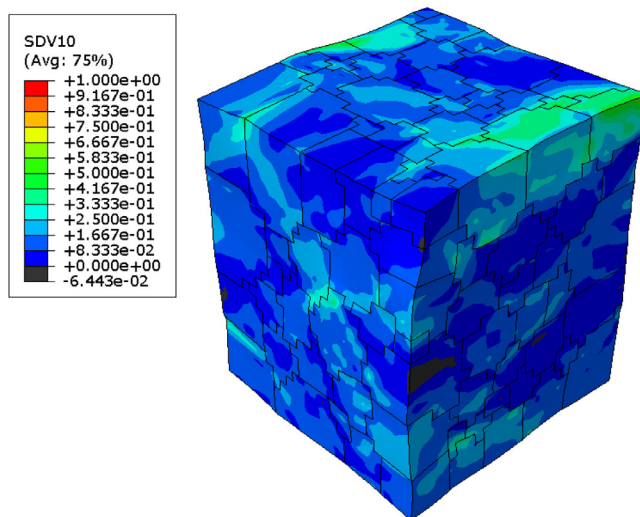


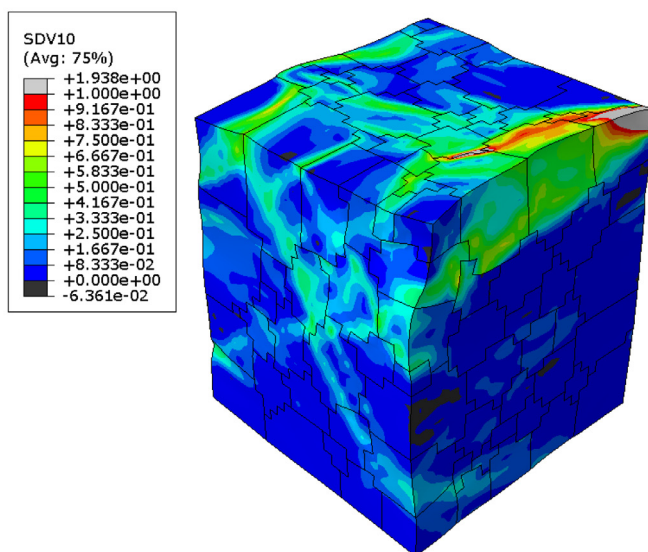
Fig. 1. Engineering stress-strain curves for Zircaloy-4 in unirradiated, 0.001 and 0.8 dpa conditions, comparing experiment (data points) from [2] and simulation using ISO-LH (solid lines), ANI-LH (dashed lines) and ANI-GND (dotted lines) models.



a. Unirradiated 0 dpa



b. Irradiated 0.001 dpa



c. Irradiated 0.8 dpa

Fig. 2. Simulation results using the ISO-LH model, showing the total plastic strain plotted on the surfaces of the cube deformed to an engineering strain of 0.1, for the conditions of (a) unirradiated, (b) Irradiated to 0.001 dpa and (c) Irradiated to 0.8 dpa.

difference in the strain distribution between the unirradiated (0 dpa) and 0.001 dpa case, however the strain in the high dose, 0.8 dpa case is highly localised. Highly localised strain was also observed for the 0.8 dpa case simulated with ANI-LH and ANI-GND models.

The engineering stress-strain results from the simulation represented the experimental behaviour relatively well after crude fitting using the parameters described above. The primary exception was that the simulation clearly overpredicted the strain softening for the 0.001 dpa condition. This is likely due to the limitations in the information about the microstructure that was produced by TEM. Irradiation to a dose of 0.001 dpa is far below that required for cascade overlap, thus the lattice damage produced is predominantly sub-nanometre ‘primary’ defects following single cascade events [46,47]. As demonstrated for irradiated tungsten [48], the majority of defects produced in single damage cascades is invisible in TEM, which suggests that the defect microstructures reported in the study by Farrell et al. likely fails to include a significant amount of lattice damage that contributes to the hardening at 0.001 dpa. In addition to lattice damage, irradiation of Zircaloy has caused chemical changes to the secondary phase precipitates [18] and matrix segregation [49], which may have a significant contribution to irradiation hardening. The amorphization of intermetallic precipitates observed after irradiation at low temperatures (< 600 K) is likely to have occurred to the material tested within the study by Farrell et al. which was irradiated at a temperature < 373 K. Only results from diffraction contrast imaging were reported in the study by Farrell, thus no information on microchemical changes was available. The hardening coefficients associated with the loop population of $H = 1.4$ (for the ISO-LH model) and $H = 1.25$ to 1.875 (for ANI-LH and ANI-GND models) used to fit the data is very large given an impenetrable discrete obstacle has a value of 1, which also suggests that other irradiation hardening mechanisms, in addition to the lattice damage visible in the TEM, may exist.

The sharp yield drop observed in the tensile data for the material irradiated to 0.8 dpa has been observed in several studies and dislocation channelling is commonly used to explain this feature [4,11]. The initial high rate of softening during the onset of plastic deformation is described as a yield drop here, because of the marked change in softening rate immediately after yielding. As seen in Eq. (18) the rate of potential annihilation events should vary as a smooth function proportional to the square root of the loop density. Given that there is little physical argument for a variation in the annihilation probability with strain, this observation suggests that annihilation probabilities may depend on different reaction types as shown by atomistic modelling [20,21]. Indeed, the yield drop behaviour was reproduced by the models which account for anisotropic dislocation-defect interactions, even with the basic approach distributing the various reactions into two groups based on the reaction segment Burgers vector. It should be noted that the increased softening evident in the latter part of the stress-strain response for the 0.8 dpa condition is almost certainly related to sample necking; this behaviour is strongly influenced by the sample geometry and the CPFEM model is therefore not expected to reproduce this effect.

4. Strain distribution analysis

4.1. Displacement boundary conditions, polycrystal model and meshing properties

The simulation work described in the previous section demonstrated that the model appears to have the correct functionality to capture the irradiation hardening, strain softening, and strain lo-

calisation commonly observed in irradiated metals. In this section we describe the use of HRDIC and EBSD data for unirradiated and proton irradiated polycrystal Zircaloy-4 [15], for direct comparison of the strain distribution measured experimentally with that predicted by the model. A full description of the experimental method is given in [15] and only details that are pertinent to the current investigation are described here. The experimental data is available in [50].

The data used for the current simulations were from Zircaloy-4 subjected to tensile loading to a final strain of ~2.3% after unloading. The raw HRDIC and EBSD data were prepared using the DefDAP python library [51], which included affine transformation of corresponding EBSD data to the DIC reference frame and cropping to selected regions of interest (ROI). The crystal morphology and orientations were represented within an FE model by use of bespoke python code. The 2D crystallographic information was extruded to produce a 3D FE model with finite thickness that is approximately representative of the surface. Finally, the experimentally measured displacements at the edges of each ROI were corrected to remove rigid body movement and were directly applied to the edge nodes of the model. The displacement boundary conditions were applied linearly over a duration of 131 s to approximately match the strain rate of the experiment. An example of a displacement boundary for the top edge of an irradiated region is given in Fig. 3. This figure shows the raw HRDIC displacement data u and v , the interpolated values and post simulation output for the nodes at the corresponding surface. Inset maps showing the corresponding maximum shear strain data highlight the discontinuities in displacement where localised slip bands intersect the edge of the ROI. The post simulation output is shown to validate that the boundary conditions were applied correctly to the model.

For both experimental data and the simulation results, the maximum shear strain in the surface plane of the material was calculated as

$$\gamma_{\max} = \sqrt{\left[\frac{1}{2}(E_{xx} - E_{yy})^2 + E_{xy}^2\right]} \quad (21)$$

where E is the Green-Lagrange strain tensor and indices x and y correspond to the horizontal and vertical directions on the surface respectively.

The influence of approximating the experiment by extrusion of the crystallography and displacement boundary conditions normal to the surface was investigated by conducting simulations of varying thickness. A $49 \times 49 \mu\text{m}$ region in the unirradiated part of the tensile specimen was selected and modelled with thicknesses of 1, 2, 5, 10 and 20 μm . A global maximum element size of 2.5 μm was prescribed, however an average element size over the surface was much smaller than this (0.5 to 1 μm) was required to accurately capture the shape detail at the grain boundaries. The elements through the thickness were equally distributed with a maximum length of 2.5 μm . Simulations were conducted using the unirradiated and irradiated polycrystals using the ISO-LH model described in Section 2 and the strain distributions predicted by each simulation are shown in Appendix A.

Minor differences were apparent between models with varying thicknesses in the simulations with unirradiated material properties, however the influence of thickness for the irradiated material properties was significant, with an increase in strain localisation with decreasing model thickness. To maintain compatibility of total strain, the mismatch between plastic strain accommodated by differing slip orientations either side of grain boundaries must be complimented by elastic strain; the resultant stresses likely in-

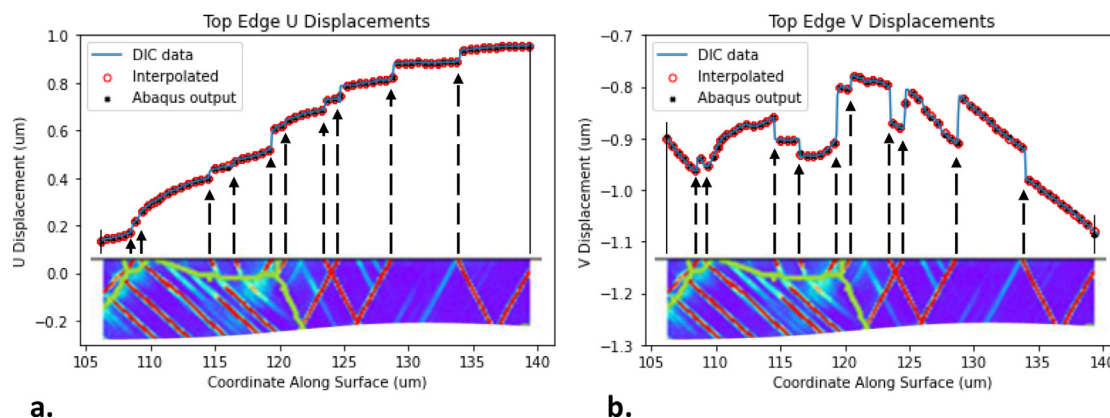


Fig. 3. Displacement boundary conditions (a) u and (b) v of the top edge of an irradiated region, showing the DIC raw displacement data, interpolated values, and simulation output called 'Abaqus output' for each node at that surface. The plots include the max shear plot in the same location indicating the link between shear band and displacement steps.

crease with thickness and competes with the softening and strain localisation. The error in extrusion of grain boundaries and edge displacement boundary conditions increases with increasing model thickness. Thus, a thickness of 2 μm was chosen for simulations of the current experiment.

A similar study was conducted to investigate the influence of mesh density on the maximum shear strain distribution for both unirradiated and irradiated material models. Very little difference in the strain distribution was observed for the mesh densities investigated. The grain boundary definition required a relatively fine mesh with element sizes of approximately 0.5 μm in length, thus this was determined to be satisfactory.

The model polycrystal microstructures were produced with a model thickness of 2 μm and mesh refinement around the centre grain with an element size of 0.5 μm or smaller. Simulations were produced with the ISO-LH, ANI-LH and ANI-GND models with all parameters as determined from the coarse fitting of stress-strain data described in Section 3. Previous XRD experiments on the material measured an area dislocation density of between 2 and 4 $\times 10^{14} \text{ m}^{-2}$. By approximating the dislocations as circular loops, dividing this by pi gives a value of dislocation density, ND , between 63 and 128 μm^{-2} . Since the value of ND used in simulations described in Section 3 was 85.4 μm^{-2} for the material neutron irradiated to 0.8 dpa, this value was also used for the simulation of the experimental polycrystal loading. Unfortunately, neither useful stress nor load data were available for the experimental irradiated material, because the irradiated region was only a small part of a much larger unirradiated specimen, thus absolute values for ND and indeed H cannot be validated and thus hold less importance for the current study which focuses on strain distribution. The irradiation depth produced by the protons was approximately 30 μm , with a uniform damage profile over the first 20 μm . Given that the average grain diameter of this alloy is 9 μm , the irradiation extends approximately three grains in thickness, thus the underlying unirradiated material is assumed to have little influence on the measured strains at the surface.

4.2. Comparison of simulations of unirradiated and irradiated polycrystal Zircaloy-4 using the ANI-LH model

Assessment of the model performance in predicting the strain distribution measured by experiment was conducted to investigate the influence of microstructure (grain morphology and crystallography) on associated strain heterogeneity. Multiple polycrys-

tal model regions, all of which include a substantive central single crystal, were developed by systematically expanding the region of interest to include adjacent grains. This was carried out for both the unirradiated and irradiated representations of the experimental microstructures. High fidelity displacement boundary conditions for each polycrystal model were available from the HR-DIC experimental measurements such that the kinematically controlled response, the behaviour of the centre grain, and progressively the role of the surrounding microstructure, were systematically studied. The various ROIs chosen and modelled from the unirradiated and irradiated experimental datasets, are shown in Fig. 4(a) and (c), respectively in which the red broken lines indicate the selected boundaries of the three model ROIs, A, B and C, considered for each case. The unidirectionally rolled texture of the experimental polycrystal samples with respect to the test loading direction are such that the prismatic and pyramidal slip systems are anticipated to be most favourably orientated for activation. The ROIs for both unirradiated and irradiated samples were selected so that the centre grain was a similar orientation, with a close competition between a prismatic and pyramidal slip systems.

Schmid analysis to identify the slip systems likely to be activated was conducted by approximating the stress in each grain to be identical to the uniaxial stress developed globally by the remote displacement loading. The 'proximity' of each slip system to activate was calculated by:

$$\zeta^k = \frac{m^k}{\tau_c^k} \quad (22)$$

where m^k is the Schmid factor and τ_c^k is the CRSS for each slip system k in the model. The slip systems with the highest 3 values of ζ^k were plotted and compared to the experiment and model results. The plots show the corresponding slip traces predicted on the surface of the specimen for each grain, from the projection of the slip plane onto the sample free surface giving vector directions calculated by:

$$\mathbf{c}^k = \mathbf{n}^k \times \mathbf{e}_z \quad (23)$$

where \mathbf{e}_z is the base vector for the specimen surface normal along the z axis (0 0 1).

The comparison between experimental and calculated in-plane shear strains for regions A of the unirradiated and irradiated sam-

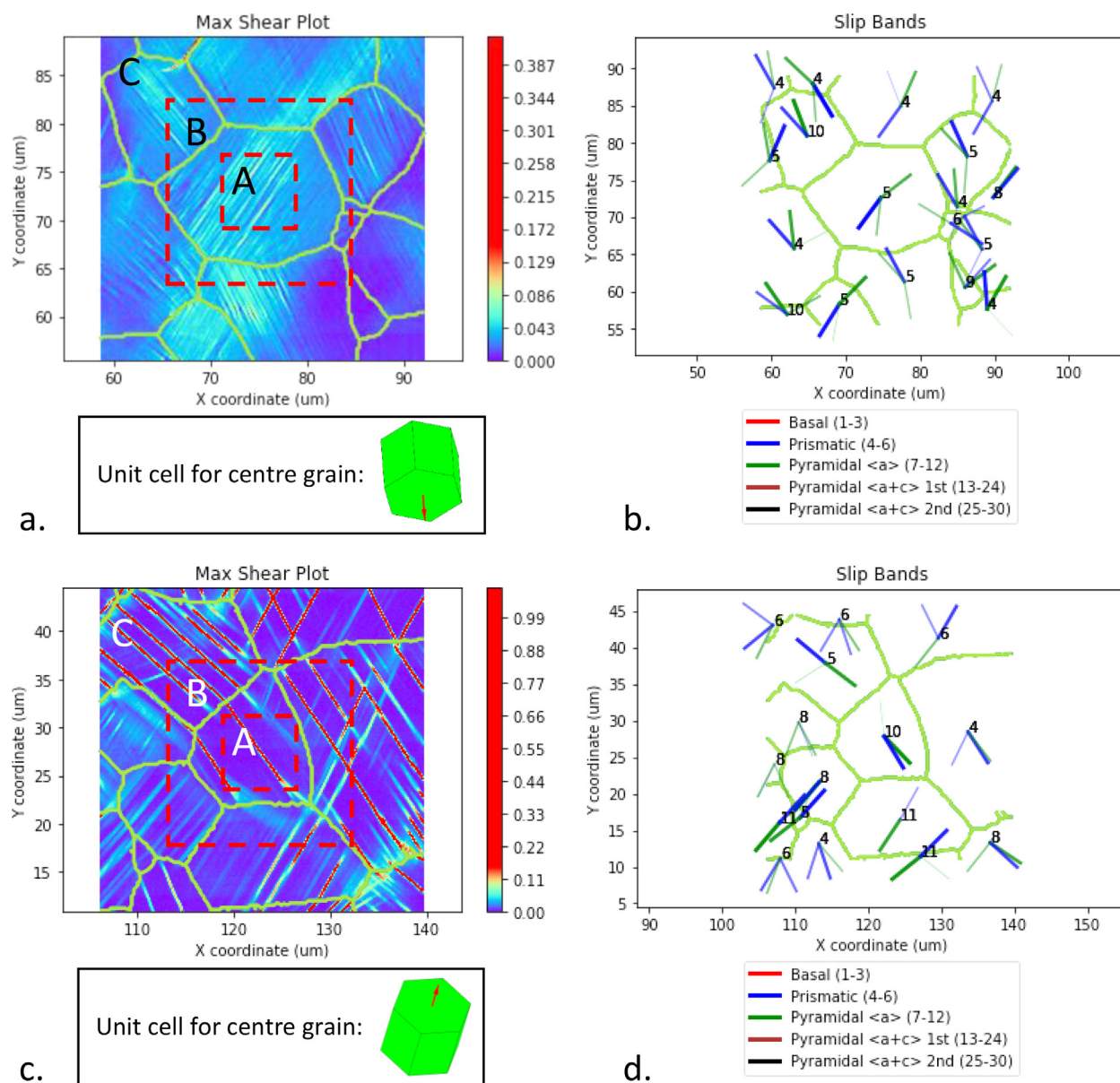


Fig. 4. Experimental measurement of maximum shear strain with simulation sub-regions indicated for (a) unirradiator and (c) irradiated areas of the specimens, with Schmid analysis showing 3 slip systems closest to activation for each grain in (b) and (d) respectively. The slip systems closest to activation are represented by lines indicating the slip trace direction on the surface with the thickness of the line proportional to the proximity of the system to be activated (ζ^k). Colour bar ranges from 0 to 0.15 maximum shear strain for all plots.

ples are shown in Fig. 5. In the unirradiator case, the slip trace directions predicted by the simulation appear not to be the same as observed in the experiment. The most active slip system calculated by the CPFEM model was prismatic $k = 5$, which was predicted by the Schmid analysis with $\zeta^5 = 216 \text{ kPa}^{-1}$ and is also apparent in the experiment (indicated in Fig. 4). However more discrete slip on the pyramidal slip system $k = 11$ (with $\zeta^{11} = 198 \text{ kPa}^{-1}$) was also calculated by the CPFEM model and is superimposed onto the maximum shear strain field (Fig. 5). In the irradiated case, although the slip trace is initiated in the correct location at the edges of the model, it is immediately obvious that the slip band direction in the model does not capture fully the experiment. The angle between the slip band and the horizontal is $\sim 55^\circ$ in the experiment, however the calculated angles that the pyramidal and prismatic systems should make are

$\sim 45.7^\circ$ and $\sim 58.6^\circ$ respectively according to the orientation measured by EBSD. The values of slip proximity for both slip systems are $\zeta^{10} = 213 \text{ kPa}^{-1}$ and $\zeta^4 = 211 \text{ kPa}^{-1}$, thus they are in very close competition yet only pyramidal slip system 10 was activate in the CPFEM model. Discrete slip is calculated by the CPFEM model for both unirradiator and irradiated cases, but the number and intensity of slip traces is incredibly different. Discrete slip in the unirradiator case is the result of imposing the displacement boundary conditions measured by HR-DIC at the edges of the model, whereas the more localised discrete slip in the irradiated case is the result of a combination of both the displacement boundary conditions and softening behaviour in the CPFEM model. The extent to which the displacement boundary conditions influence the calculated strain distribution becomes evident in the simulation results for the larger ROIs B and C.

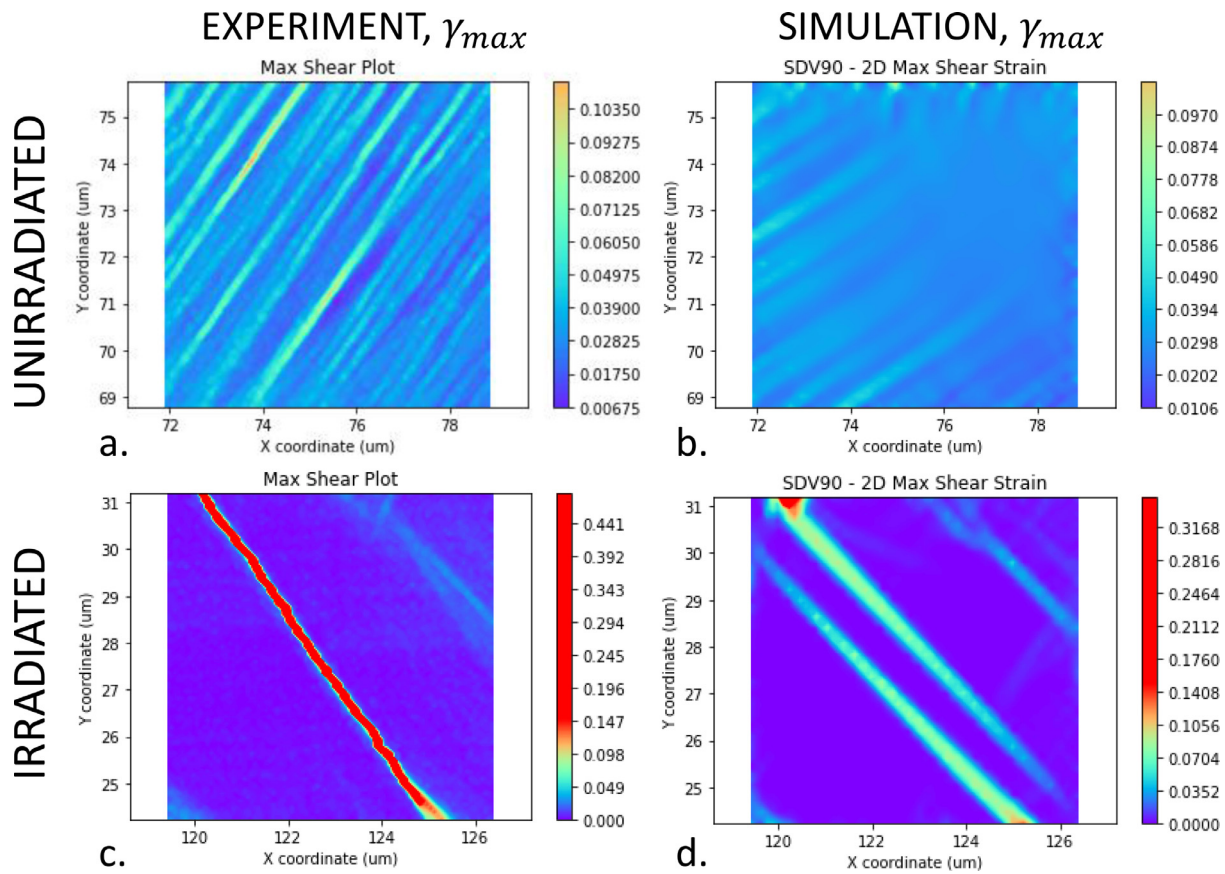


Fig. 5. Regions A in the unirradiated and irradiated condition, showing the maximum shear strain measured by experiment (a. and c. respectively) and predicted by simulation using the ANI-LH model (b. and d. respectively). Colour bar ranges from 0 to 0.15 maximum shear strain for all plots.

The comparison between experimental and simulation results for regions B of both unirradiated and irradiated Zircaloy-4 are shown in Fig. 6. In the unirradiated case, the activation of slip systems 4 and 5 calculated by the CPFEM model agrees with the slip systems identified from the Schmid analysis. The grain in the top left corner of this region had highest slip proximity for pyramidal system $k = 10$, however in the experiment the angle of shear bands is clearly aligned to the prismatic slip system $k = 4$ which is also active in the simulation for this grain. Again, the localised slip at the bottom of the simulated shear strain map, indicated by a black arrow in Fig. 6b, results from the HR-DIC experimentally measured displacements which provide the displacement boundary conditions for the simulation, but the strain in the centre grain is less discrete showing a reduction in kinematically controlled deformation away from the edges. In the irradiated case, the localised slip in the simulation represents the experimental measurement well, with the orientation of slips traces in agreement with the experiment for many edge grains. Again, the centre grain has deformed predominantly by slip on the pyramidal system $k = 10$, which is the same as that predicted by the CPFEM model for region A (Fig. 5).

The comparison between experimental and simulation results for regions C of the unirradiated and irradiated conditions are shown in Fig. 7. The extent of strain accommodated by slip systems 4 and 5 was the same as in region B, showing that the predictions of slip calculated by the CPFEM model are largely what is expected according to the Schmid analysis, however the discrete slip bands

in the grain at the bottom of region B are no longer present in the simulation of region C due to the larger distance of this location to the kinematically controlled deformation at the edge of the model. Discrete slip is less obvious at the edges of region C, which is likely due to a coarser mesh applied at the edges of this model which is away from the refined mesh around the centre grain. As identified for region B in the irradiated case, many of the localised slip bands agree with the experiment apart from the centre grain, which appears to be nearly entirely accommodated by pyramidal system $k = 10$. In general, the plasticity is accommodated by fewer slip bands in the centre grains, which may indicate that the hardening of individual slip bands is insufficiently captured in the CPFEM model. Approximating the experiment by modelling a thin sheet likely underestimates the constraint imposed by the underlying microstructure which exists in the experiment, which gives rise to fewer, more intense slip bands as shown in the thickness sensitivity study in Appendix A.

Both the unirradiated and irradiated regions simulated were selected to have a centre grain with close competition between prismatic and pyramidal slip. For the unirradiated case the primary activated slip system calculated by the CPFEM model agreed with the experimental observation, yet the pyramidal slip system was also activated in the simulation. In the irradiated case pyramidal slip was predicted by the simulation in contrast to prismatic slip observed in the experiment. This may indicate that the CRSS of pyramidal slip is too low in the model relative to prismatic slip.

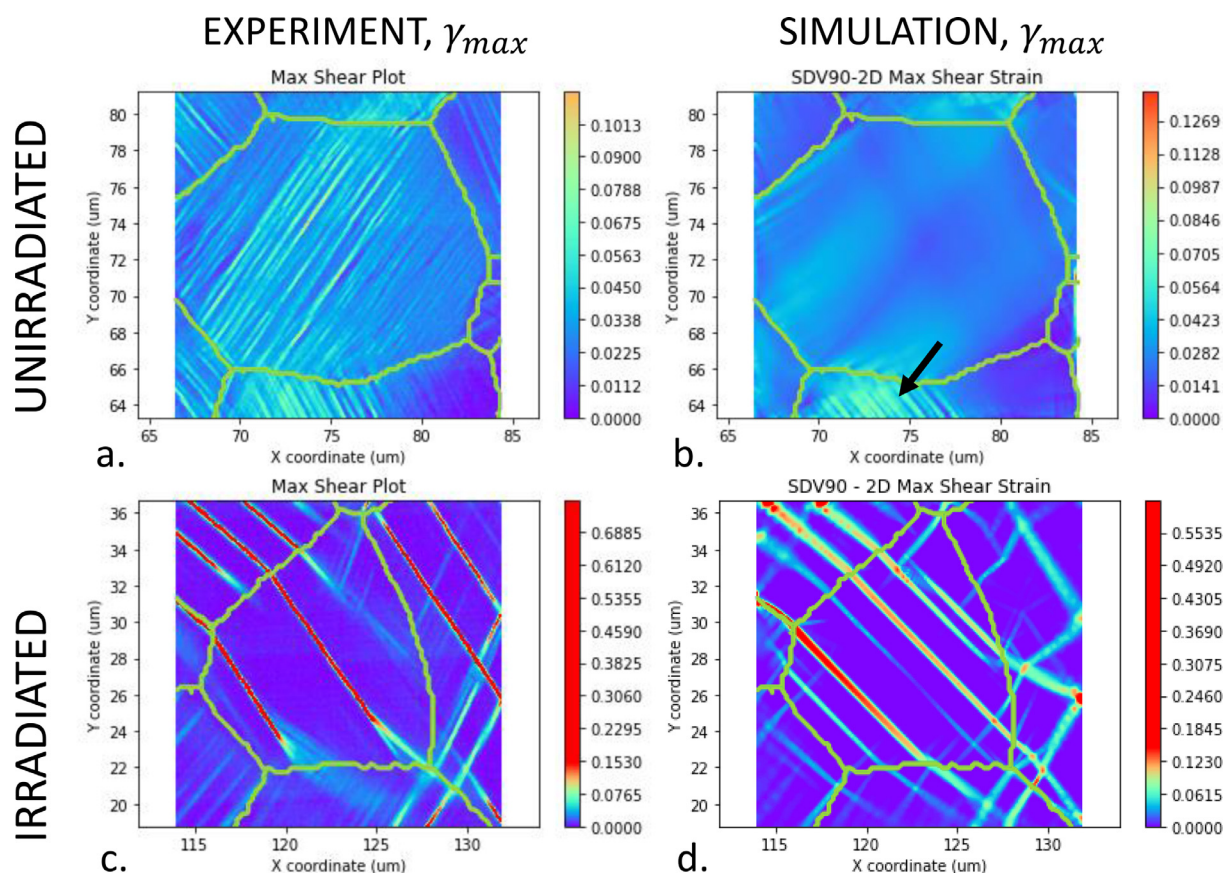


Fig. 6. Regions B in the unirradiated and irradiated condition, showing the maximum shear strain measured by experiment (a. and c. respectively) and predicted by simulation using the ANI-LH model (b. and d. respectively). The black arrow in (b) indicates localised slip resulting from the displacement boundary conditions. Colour bar ranges from 0 to 0.15 maximum shear strain for all plots.

The likelihood of prismatic and pyramidal slip was calculated to be nearly identical for the centre grain in the irradiated ROI. The angle of the associated slip band measured from the experimental data was between that calculated for both systems. Given the strong agreement between experiment and simulation in slip band orientations for most grains in the larger simulations, this difference cannot be attributed to error in the measured orientation by EBSD. The slip band may have been formed by multiple cross-slip between both systems, where the latter has been observed experimentally for titanium [52]. Given that activation of just one slip system was predicted by the CPFEM model, the consequences of potential cross-slip observed experimentally is not represented in the simulation results for region A. This may suggest that the components of strain hardening and/or radiation hardening which evolve within the hardening law are insufficient to capture this borderline case.

Due to the applied deformation along the rolling direction, prismatic and pyramidal slip were the only slip systems activated and observed experimentally and predicted by CPFEM simulation in the regions investigated. No twinning was observed in the experiment; thus, twinning was not enabled in the CPFEM model. The active slip systems predicted by the CPFEM simulation of both unirradiated and irradiated regions agreed well with the Schmid analysis and that observed experimentally for most grains.

For the unirradiated region C, the strain distribution predicted by the simulation using the ANI-LH model represents that measured in the experiment relatively well (Fig. 7). The magnitude of the shear strain appears higher in the experiment, because the de-

formation comprises highly strained discrete slip bands with fine spacing, in contrast to more diffuse deformation predicted by the simulation. The model cannot capture the discrete slip measured by HRDIC in the experiment in the unirradiated material, because the CPFEM formulation does not capture the discrete dislocation slip mechanisms associated with dislocation source activation and corresponding non-monotonic stress-strain response of individual slip systems.

The strain distributions predicted by the simulations of the irradiated regions are highly localised, due to the softening caused by modelling defect annihilation. The exact locations of the slip bands are influenced by slip transfer across grain boundaries and invisible or sub-surface microstructural features that are not represented in the model.

Simulation results for the irradiated region C showing the total dislocation loop density and loop densities for loops with Burgers vectors in each of the 3 $\langle a \rangle$ directions are shown in Fig. 8. The simulation was conducted with the anisotropic dislocation-loop interaction model (ANI-LH); thus, dislocation loop densities vary for each of the 3 loop types dependent on the interactions between the active slip systems and loop types for each grain. The resulting total dislocation loop density consists of dislocation channels which are partially cleared of dislocation loops. This result compares well with the description of channel clearing identified by Onimus et al. that in contrast to basal channels, prismatic and pyramidal channels were only partially cleared of defects [14]. TEM observations of the post deformation microstructure are not yet available for the material studied here, however comparison of

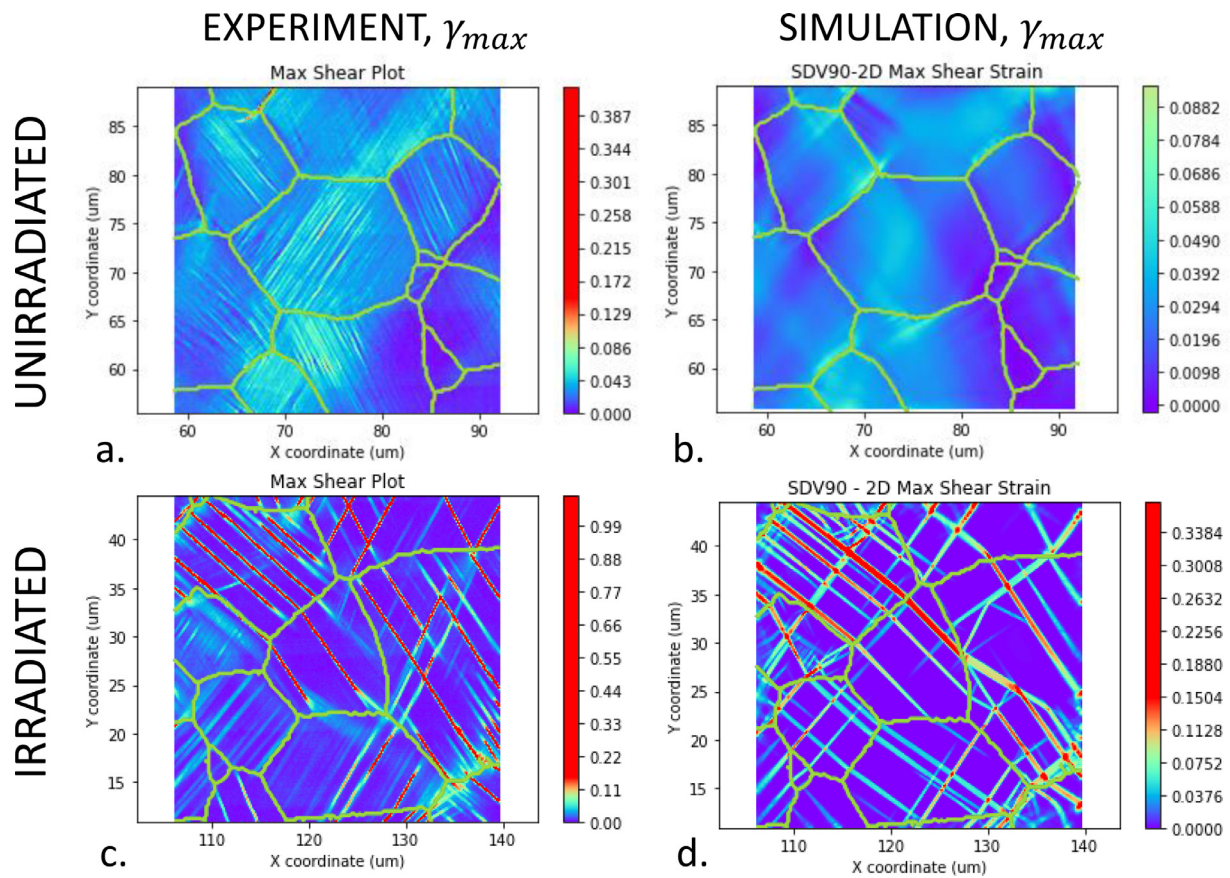


Fig. 7. Regions C in the unirradiated and irradiated condition, showing the maximum shear strain measured by experiment (a. and c. respectively) and predicted by simulation using the ANI-LH model (b. and d. respectively). Colour bar ranges from 0 to 0.15 maximum shear strain for all plots.

such observations and the simulated dislocation loop density distribution would be very useful for model validation and is thus planned as future work.

4.3. Comparison of ISO-LH, ANI-LH and ANI-GND models

Fig. 9 shows a comparison of the maximum shear strain and total dislocation loop densities produced by simulations for the irradiated region C using the ISO-LH, ANI-LH and ANI-GND models. The ISO-LH model with isotropic dislocation-defect interaction has fewer localised slip bands with higher peak strain compared to the ANI-LH model. In contrast to partially cleared channels exhibited by the ANI-LH model, many of the slip bands in the ISO-LH model are completely cleared of dislocation loops. This difference in dislocation channelling behaviour compares well to the experimental observation of partial clearing in prismatic and pyramidal systems in contrast to full clearing in basal channels in irradiated Zr alloys [14], alongside a transition in the predominant slip system from prismatic to basal following irradiation in many Zr alloys [8,14]. Although the experiment and corresponding simulations conducted in this study were on an orientation that did not involve basal slip, the dislocation-defect interaction rule used here would likely account for this experimental observation. All dislocation reaction segments produced by dislocations gliding in the basal plane remain in the basal plane, thus the anisotropic dislocation-defect interaction model represents lower irradiation hardening and higher defect annihilation probabilities on basal systems. This will be investigated as part of future work. The maximum shear strain distribution predicted by the model

based on strain hardening by GND density (ANI-GND) is more diffuse, with localised slip bands of much lower peak strain. The corresponding dislocation density plot includes some partially cleared dislocation channels and large areas of partial clearance. Many of the slip bands appear wavy in nature and further investigation of the simulation results showed that multiple slip systems are activated in each grain. It is likely that the activation of multiple slip systems is encouraged in the ANI-GND model because the high strain gradients associated with localised slip via a single slip system, result in high densities of GNDs and strain hardening. The obstacle strength used to fit the stress-strain data for strain hardening by GNDs in Section 4 was $\alpha^2 = 0.05$, which is equivalent to $\alpha > 0.2$ if considered in isolation and outside the square root (as conventionally used in a Taylor hardening equation). This is a very high value; thus, it is likely that strain hardening may be a mixture of GND and statistically stored dislocation (SSD) densities, and that the influence of GND density is too high in the model used here.

On inspection of the maximum shear strain maps produced by all three models, it is apparent that many slip bands are accommodated by perpendicular slip activations in each grain. Most apparent in the ANI-LH model results, further investigation highlighted that these perpendicular slip bands are a result of slip from a single slip system. This deformation mechanism is effectively localised kink band formation and has been demonstrated in CPFEM simulations of softening metals extensively by Marano et al. [53]. The formation of localised kink bands in irradiated materials is energetically unfavourable, since this mechanism requires the activation of many dislocation sources in adjacent planes in close prox-

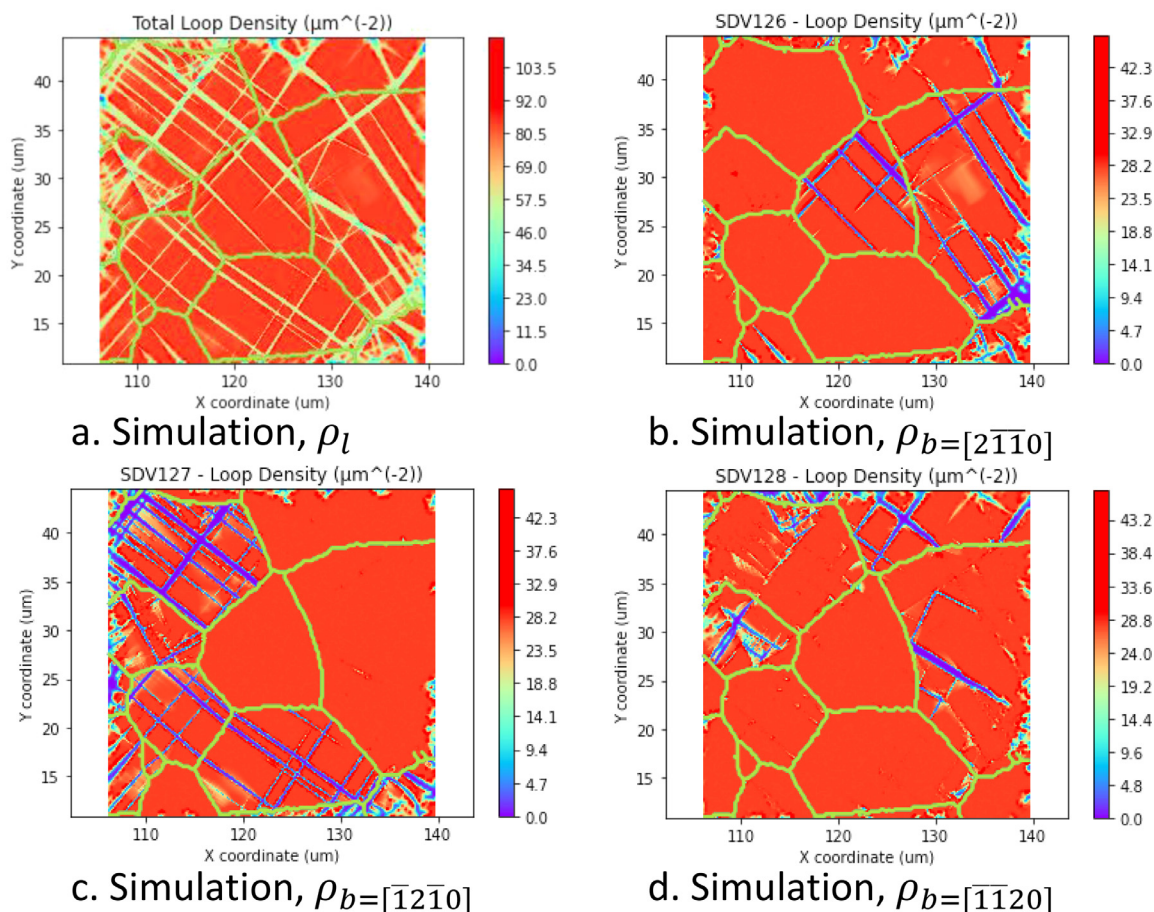


Fig. 8. Simulation results for the irradiated Zircaloy-4 produced by the ANI-LH model, showing total dislocation loop density (a) and dislocation loop densities for loops with Burgers vectors in each of the 3 $\langle a \rangle$ directions (b, c & d).

imity. Thus, it is not observed in the experimental data shown here for Zircaloy-4, nor in many experimental studies of irradiated metals. The localised kink band formation predicted by the model is essentially an artefact resulting from the local continuum CPFEM formulation which cannot account for the geometric influence of dislocation source activation across a slip plane. In earlier work Marano et al. [53] hypothesised that the use of a strain hardening model based on GND density may reduce kink band formation in simulations due to their associated high lattice curvature, yet this was not observed in our simulations using the ANI-GND model. It was later shown by the same authors that the curl of the plastic deformation gradient (as described in Eq. (5)) has the same order of magnitude for both slip and kink band deformation for the majority of cases, thus higher order (double curl) differentiation was required to penalise kink band formation [54]. Whilst effective in achieving a more representative prediction of deformation behaviour qualitatively, i.e., by promotion of slip band over kink band formation, the variants of curl operations [55] and many variants of higher order operations, and their physical relevance to dislocation slip mechanisms remains an important subject of debate.

Modelling anisotropic dislocation-defect interactions resulted in an increase in the number of bands, which is closer to that observed in the experiment. This demonstrates the influence slip system shear stress-strain response has on the plastic strain distribution, where softening initiates local slip and subsequent hardening

determines the extent of slip before activation of adjacent bands becomes more favourable.

5. Conclusions and outlook

The purpose of this study was to investigate the adequacy of CPFEM to simulate strain softening and localisation in irradiated metals.

- A new CPFEM formulation to account for the effect of irradiation is presented, which is physically based on dislocation mediated plasticity and consistent with an established slip law. This model captured irradiation hardening due to the introduction of radiation defects (in the form of dislocation loops in the present study) and strain softening arising from defect annihilation as a function of the various interactions between gliding dislocations and dislocation loop burgers vectors. The latter was derived based on the geometrically controlled average rate of dislocation-defect interactions as a function of plastic slip rate and defect density.
- A mixed superposition hardening law was proposed that accounted for strengthening by both lattice friction and discrete obstacles, which was essential to reproduce the irradiation hardening (increase in yield stress) and subsequent strain softening with constant parameters for the two irradiation conditions studied.

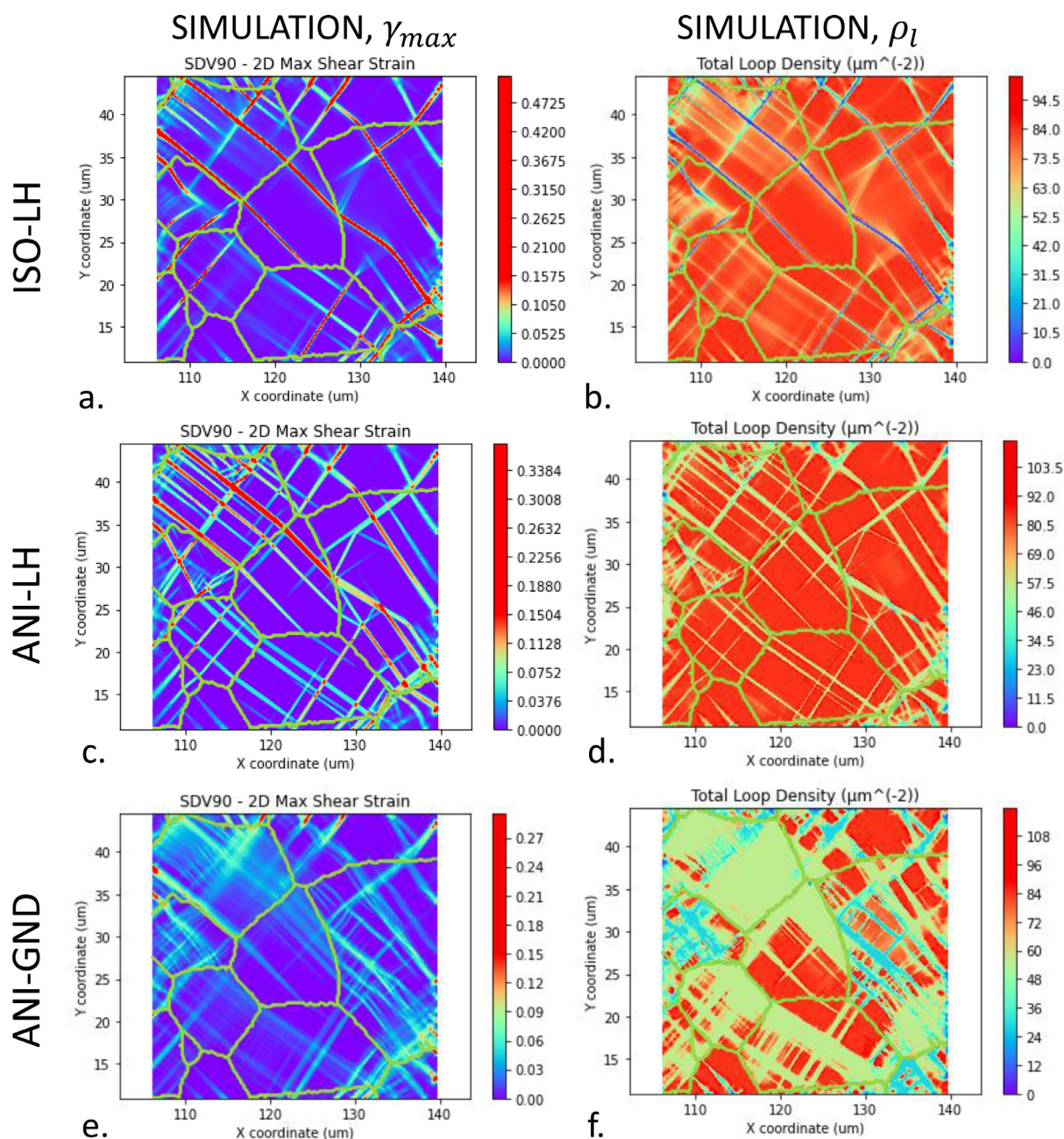


Fig. 9. Simulated maximum shear strain and total dislocation loop density for the irradiated region C, produced from the ISO-LH (a and b), ANI-LH (c and d) and ANI-GND (e and f) models. Colour bar ranges from 0 to 0.15 maximum shear strain for (a, c and e) and from 0 to 90 μm^{-2} loop density for (b, d and f).

- Variants of the model based on strain hardening proportional to effective plastic strain or proportional to GND density evolution, and isotropic or anisotropic dislocation-defect reactions (determining hardening and annihilation) were compared. We show that the treatment of the different reaction paths between gliding dislocations and radiation defects (the ANI- models) is essential to accurately capture the varying strain softening rate, notably a yield drop, observed in Zircaloy-4 and common to many irradiated metals.
- Novel methods were developed to extract high fidelity displacement boundary conditions from experimental displacements measured by HR-DIC, and coupling with corresponding crystal morphology and orientations from the same selected region captured by EBSD data. The direct simulation of experiments

highlighted the ability of the new CPFEM model to capture the extraordinary discrete slip localisation in irradiated material, in contrast to diffuse slip in the unirradiated material. The localised strain predicted by all models consisted of dislocation slip bands and localised kink bands, where the latter was not observed experimentally. Further work is required to develop the model to better represent the physical mechanisms of plastic deformation.

It is clear from this study that the simulation of strain softening and localisation in irradiated metals is sensitive to the treatment of the various microstructural hardening constituents and their evolution with plasticity. Accounting for the multitude of deformation processes that occur during plasticity, necessitates a

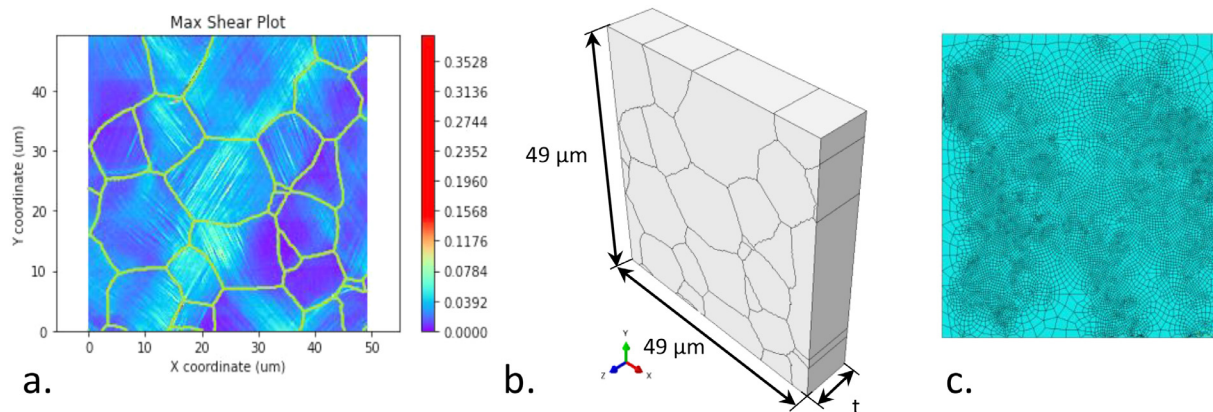


Fig. 10. Experimental measurement of max shear strain measured by HRDIC from a region of the unirradiated part of the tensile test (a), model geometry showing thickness dimension (b) and image of the surface mesh (c).

multi-parameter model with many degrees of freedom; this in turn requires extensive experimental data for satisfactory parameterisation. The model can be calibrated to fit a given experimental dataset with relatively simple formulation (e.g. CRSS evolution in [35]), however a genuine predictive capacity requires data from multidimensional experiments, including temperature, strain rate and radiation damage microstructures. The parameter sensitivity study presented in Appendix B highlights the influence of each deformation process and their relative interdependencies for a single slip system. This study highlights the competition between hardening and softening as a function of strain in a single slip system, which in the case of the irradiated Zircaloy-4 studied here softening is clearly dominant. Parameterisation and validation of this constitutive behaviour may therefore support assessment of a materials propensity to exhibit strain localisation and predict onset of associated premature failure in complex environments of damage, temperature, and cyclic loading.

It is very important that the irradiation damage microstructure is sufficiently characterised, so that the various strengthening constituents are represented correctly in the model. In addition to the rich data acquired by HRDIC experiments, micro-mechanical testing would be very valuable to measure the slip system specific CRSS as a function of strain for the various conditions. Atomistic scale modelling can also provide valuable insights, particularly on dislocation-defect interactions, which can infer relative obstacle strengths and annihilation probabilities. A fully parameterised CPFEM model validated with experiments will provide a predictive capability for reactor environments that are difficult or impossible to represent experimentally. This will provide a much-needed means of predicting material behaviour across a wide range of radiation conditions including various doses and temperatures and operating conditions including creep and cyclic loading. An example of successful application of a similar model is given in [23], where microstructurally representative crystal plasticity modelling reproduced hydride formation and resultant localised slip in the presence of cyclic loading.

Declaration of Competing Interest

The authors declare that they have no known competing financial interests or personal relationships that could have appeared to influence the work reported in this paper.

Acknowledgements

The authors gratefully acknowledge financial support from EP-SRC MIDAS Programme Grant [EP/S01702X].

Appendix A. Model Thickness Sensitivity Study

The region selected for the model thickness sensitivity study is shown in Fig. 10, with a description of model dimensions and image of the surface mesh. Thicknesses, t , of 1, 2, 5, 10 and 20 μm were modelled using the ISO-LH model and both the unirradiated and irradiated (0.8 dpa) parameters as parameterised in Section 3. A global element size of 2.5 μm was prescribed, however an average element size was much smaller than this (0.5 to 1 μm) was required to accurately capture the shape detail at the grain boundaries. Given that there was no shape detail to capture through thickness, the elements were 2.5 μm in this dimension and the number of elements through thickness varied with model thickness from 1 element for $t = 1$ and 2 μm , to 2, 4 and 8 elements for $t = 5, 10$ and 20 μm respectively. Displacement boundary conditions taken from the HRDIC measurement at the edge of the region were applied to the edge of the model.

A comparison of the maximum shear strain distribution between 1 and 20 μm thicknesses for the unirradiated and irradiated material properties is given in Fig. 11. Minor differences are apparent between the two thicknesses in the simulations with unirradiated material properties, however the influence of thickness for the irradiated material properties is striking, with an increase in strain localisation with a decreasing model thickness.

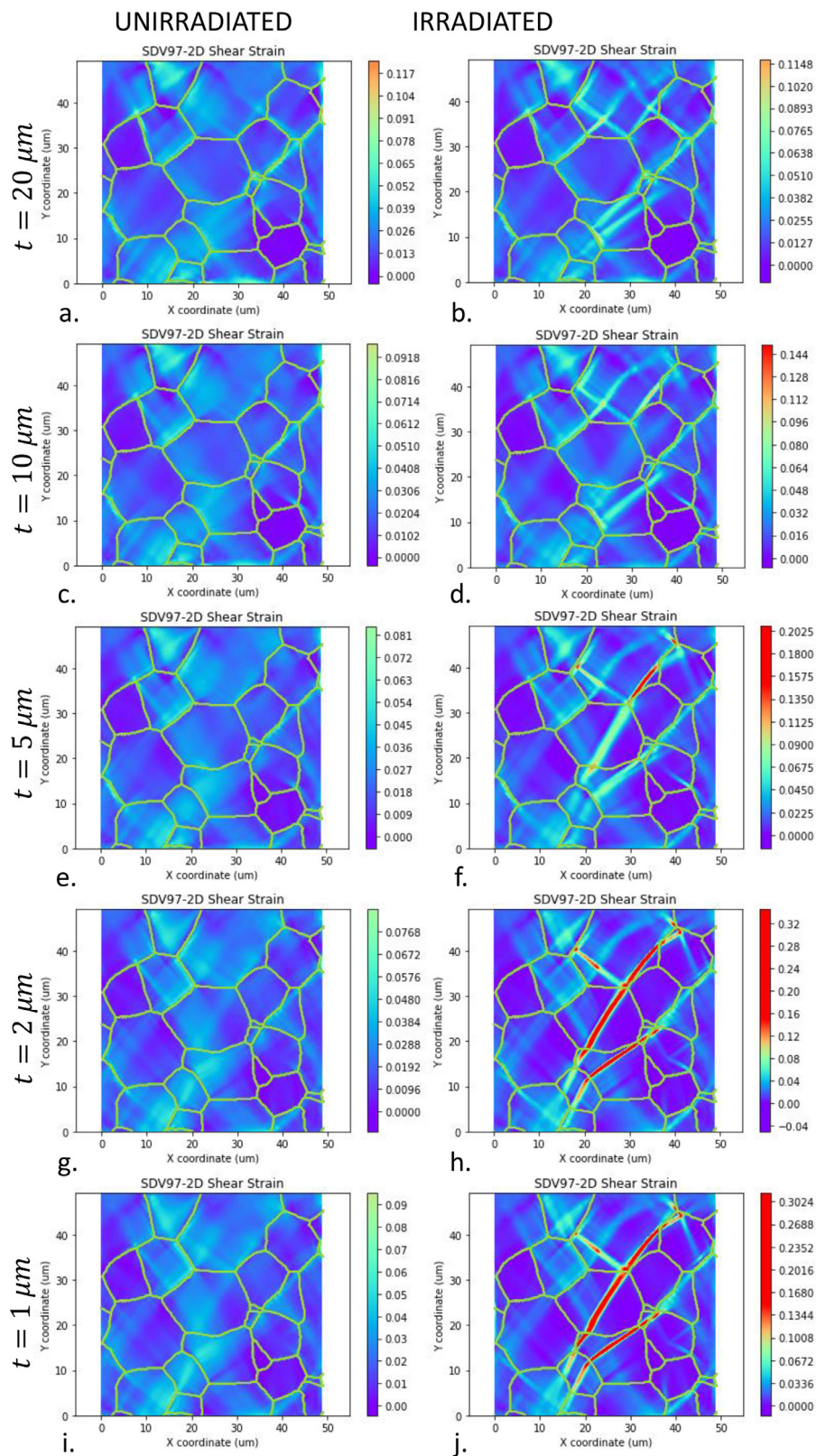


Fig. 11. Maximum shear strain produced from unirradiated and irradiated materials parameters with the ISO-LH material model, using finite element models with various thicknesses from 1 to 20 μm .

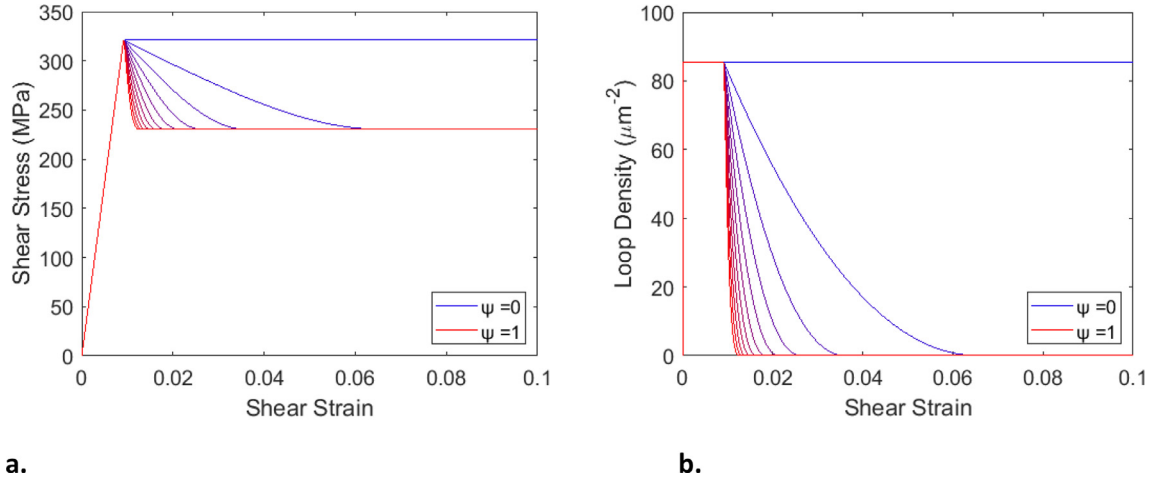


Fig. 12. (a) Shear stress-shear strain response and (b) dislocation loop density evolution for a strain rate of 10^{-4} /s for annihilation probabilities from 0 to 1.

Appendix B. Single slip system parameter sensitivity study

The effect of loop annihilation hardening parameters on slip system response was investigated using a simple implicitly integrated slip model (written in MATLAB) for a single slip system. Fig. 12 shows the effect of varying the annihilation probability, ψ , linearly from 0 to 1, which represents the probability from 0 to 100%, respectively, that a single interaction between a gliding dislocation and loop will result in removal of that loop from the lattice. For this study, the hardening law described in Eq. (3), with $\tau_0 = 228.5$, $X = 0.31$ and $Y\alpha^2 = 0.0 \mu\text{m}^{-2}$ was used, i.e., no strain hardening was considered. An initial loop area density of $N_l d_l = 85.4 \mu\text{m}^{-2}$, and a hardening coefficient of $H = 1.4$ resulted in an initial CRSS of 319.3 MPa.

Softening of the shear stress-shear strain curve and reduction in loop density with increasing strain is evident as expected. This data was produced with a strain rate of 10^{-4} /s. The reduction in loop density shown in Fig. 12b is proportional to $\gamma_p \sqrt{N_l d_l}$, which corresponds the annihilation relationship defined in Eq. (18). As discussed in Section 2, the fraction of unirradiated strength attributed to discrete obstacles is defined by parameter X in Eq. (18). The influence of the fraction X on the shear stress-strain response with a linear variation of from 0 to 1 is shown in Fig. 13.

As indicated by the reduction in yield strength, the magnitude of irradiation hardening decreases with an increasing fraction of

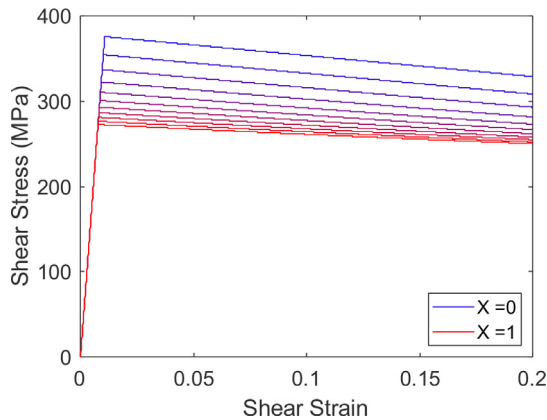


Fig. 13. Influence of the fraction of alloying strength attributed to discrete obstacles, X in the range from 0 to 1.

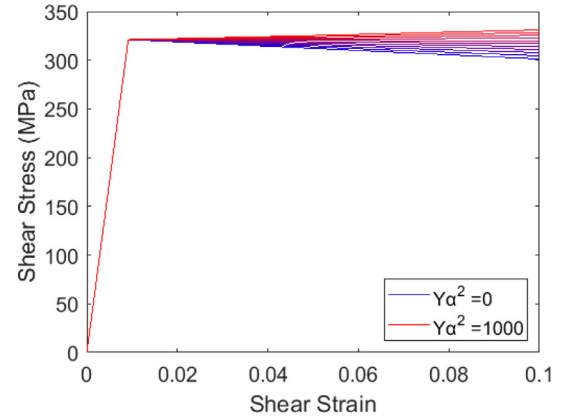


Fig. 14. Influence of the strain hardening coefficient, $Y\alpha^2$, for the linear hardening model in the range from 0 to 1000 μm^{-2} .

unirradiated strength attributed to discrete obstacles, as seen experimentally [7]. The rate of removal of defects remains unaffected, however the gradient of softening decreases as X increases. Physically, this effect is due to the reduced influence of irradiation defects in the presence of an increasing fraction of pre-existing discrete obstacles in the lattice. Finally, the influence of strain hardening coefficient was investigated for the linear hardening behaviour and is shown in Fig. 14. This result demonstrates the competition between strain hardening and softening due to the annihilation of irradiation induced defects.

By approximating the effective plastic strain as $\bar{\epsilon}_p \approx \sqrt{\frac{2}{3}} \gamma_p$, i.e. that for perfect shear, the differential of τ_c with respect to the plastic shear strain for the linear hardening model is:

$$\frac{d\tau_c}{d\gamma_p} = \frac{Gb}{2\sqrt{\left(\frac{X\tau_0}{Gb}\right)^2 + \sqrt{\frac{2}{3}}Y\alpha^2\gamma_p + H^2N_l d_l}} \left[\sqrt{\frac{2}{3}}Y\alpha^2 - \frac{H^2\psi}{b}\sqrt{N_l d_l} \right] \quad (24)$$

For the irradiation hardening and annihilation parameters used in this study, a strain hardening coefficient of $Y\alpha^2 = 693 \mu\text{m}^{-2}$ is required to counter the softening due to the annihilation of defects, which is much higher than the value of $130 \mu\text{m}^{-2}$ used to fit the unirradiated stress-strain response.

References

- [1] F.P.E. Dunne, D. Rugg, A. Walker, Lengthscale-dependent, elastically anisotropic, physically-based hcp crystal plasticity: application to cold-dwell fatigue in Ti alloys, *Int. J. Plast.* 23 (2007) 1061–1083, doi:10.1016/j.ijplas.2006.10.013.
- [2] K. Farrell, T.S. Byun, N. Hashimoto, Deformation mode maps for tensile deformation of neutron-irradiated structural alloys, *J. Nucl. Mater.* 335 (2004) 471–486, doi:10.1016/j.jnucmat.2004.08.006.
- [3] K. Farrell, T.S. Byun, N. Hashimoto, Mapping flow localization processes in deformation of irradiated reactor structural alloys, *Nucl. ENERGY Res. Initiat. Progr. Report.* 1999-2002. (2002).
- [4] T. Onchi, H. Kayano, Y. Higashiguchi, Effect of neutron irradiation on deformation behavior of zirconium, *J. Nucl. Sci. Technol.* 14 (1977) 41–51, doi:10.1080/18811248.1977.9730770.
- [5] M. Nakatsuka, Mechanical properties of neutron irradiated fuel cladding tubes, *J. Nucl. Sci. Technol.* 28 (1991) 356–368, doi:10.1080/18811248.1991.9731368.
- [6] K. Pettersson, G. Vesterlund, T. Andersson, Effect of irradiation on the strength, ductility, and defect sensitivity of fully recrystallized Zircaloy tube, in: *ASTM Special Technical Publication*, ASTM, 1979, pp. 155–173, doi:10.1520/stp36678s.
- [7] R.A. Holt, The effect of metallurgical condition and irradiation on strength and ductility of Zr-1.14% Cr-0.1% Fe, *J. Nucl. Mater.* 50 (1974) 207–214, doi:10.1016/0022-3115(74)90157-3.
- [8] F. Onimus, J.L. Béchade, C. Duguay, D. Gilbon, P. Pilvin, Investigation of neutron radiation effects on the mechanical behavior of recrystallized zirconium alloys, *J. Nucl. Mater.* 358 (2006) 176–189, doi:10.1016/j.jnucmat.2006.07.005.
- [9] B. Bose, Bipasha Bose Assessment of the kinetics of local plastic deformation of Zr-2.5% Nb CANDU pressure tube material, *Electron. Thesis Diss. Repos.* (2012). <https://ir.lib.uwo.ca/etd/446>.
- [10] H. Kayano, Y. Higashiguchi, S. Yajima, T. Onchi, Yield point phenomenon in neutron irradiated zirconium, *J. Nucl. Sci. Technol.* 15 (1978) 868–871, doi:10.1080/18811248.1978.9735603.
- [11] B. Cheadle, C. Ellis, J. van der Kuur, Plastic instability in irradiated Zr-Sn and Zr-Nb Alloys, in: *Zirconium in Nuclear Application*, ASTM International, 2009, p. 370, doi:10.1520/stp32126s. -370-15.
- [12] T. Yasuda, M. Nakatsuka, K. Yamashita, Deformation and fracture properties of neutron-irradiated recrystallized Zircaloy-2 cladding under uniaxial tension, in: *Zirconium in the Nuclear Industry*, ASTM International, 2008, p. 734, doi:10.1520/stp28156s. -734-14.
- [13] F. Onimus, J.L. Béchade, C. Prioul, P. Pilvin, I. Monnet, S. Doriot, B. Verhaeghe, D. Gilbon, L. Robert, L. Legras, J.P. Mardon, A. Motta, K. Kapoor, R. Adamson, G. Sheck, Plastic deformation of irradiated zirconium alloys: TEM investigations and micro-mechanical modeling, in: *ASTM Special Technical Publication*, American Society for Testing and Materials, 2005, pp. 53–78, doi:10.1520/stp37502s.
- [14] F. Onimus, I. Monnet, J.L. Béchade, C. Prioul, P. Pilvin, A statistical TEM investigation of dislocation channeling mechanism in neutron irradiated zirconium alloys, *J. Nucl. Mater.* 328 (2004) 165–179, doi:10.1016/j.jnucmat.2004.04.337.
- [15] R. Thomas, D. Lunt, M.D. Atkinson, J. Quinta da Fonseca, M. Preuss, F. Barton, J. O'Hanlon, P. Frankel, The effect of loading direction on slip and twinning in an irradiated zirconium alloy, in: *Proceedings of the Zirconium Nuclear Industry 19th International's Symposium*, 2021, pp. 233–261, doi:10.1520/STP162220190027.
- [16] T. Byun, N. Hashimoto, Strain localization in irradiated materials, *Nucl. Eng. Technol.* 38 (2006) 619–638.
- [17] D.J. Bacon, Y.N. Osetsky, D. Rodney, Chapter 88 dislocation-obstacle interactions at the atomic level, *Dislocat. Solids* 15 (2009) 1–90, doi:10.1016/S1572-4859(09)01501-0.
- [18] M. Griffiths, A review of microstructure evolution in zirconium alloys during irradiation, *J. Nucl. Mater.* 159 (1988) 190–218, doi:10.1016/0022-3115(88)90093-1.
- [19] K. Ghavam, R. Gracie, Simulations of reactions between irradiation induced 'a' - loops and mixed dislocation lines in zirconium, *J. Nucl. Mater.* 462 (2015) 126–134, doi:10.1016/j.jnucmat.2015.03.007.
- [20] A. Serra, D.J. Bacon, Atomic-level computer simulation of the interaction between 1/3 (1120) 1100 dislocations 1/3(112°) interstitial loops in α -zirconium, *Model. Simul. Mater. Sci. Eng.* 21 (2013) 045007, doi:10.1088/0965-0393/21/4/045007.
- [21] J. Drouet, L. Dupuy, F. Onimus, F. Momprou, S. Perusin, A. Ambard, Dislocation dynamics simulations of interactions between gliding dislocations and radiation induced prismatic loops in zirconium, *J. Nucl. Mater.* 449 (2014) 252–262, doi:10.1016/j.jnucmat.2013.11.049.
- [22] W. Wan, F.P.E. Dunne, Microstructure-interacting short crack growth in blocky alpha Zircaloy-4, *Int. J. Plast.* 130 (2020) 102711, doi:10.1016/j.ijplas.2020.102711.
- [23] Y. Liu, S. El Chamaa, M.R. Wenman, C.M. Davies, F.P.E. Dunne, Hydrogen concentration and hydrides in Zircaloy-4 during cyclic thermomechanical loading, *Acta Mater.* 221 (2021) 117368, doi:10.1016/j.actamat.2021.117368.
- [24] C. Coleman, V. Grigoriev, V. Inozemtsev, V. Markelov, M. Roth, V. Makarevicius, Y.S. Kim, K.L. Ali, J.K. Chakravarthy, R. Mizrahi, R. Lalgudi, The effect of microstructure on delayed hydride cracking behavior of Zircaloy-4 fuel cladding: an international atomic energy agency coordinated research program, *J. ASTM Int.* 7 (2010), doi:10.1520/JAI103008.
- [25] Y. Liu, W. Wan, F.P.E. Dunne, Characterisation and modelling of micro- and macroscale creep and strain rate sensitivity in Zircaloy-4, *Mater. Sci. Eng. A* 840 (2022) 142981, doi:10.1016/j.msea.2022.142981.
- [26] Y. Liu, S. El Chamaa, M.R. Wenman, C.M. Davies, F.P.E. Dunne, Hydrogen concentration and hydrides in Zircaloy-4 during cyclic thermomechanical loading, *Acta Mater.* 221 (2021) 117368, doi:10.1016/j.actamat.2021.117368. ISSN 1359-6454
- [27] J. Gong, T. Benjamin Britton, M.A. Cuddihy, F.P.E. Dunne, A.J. Wilkinson, (a) Prismatic, (a) basal, and (c+a) slip strengths of commercially pure Zr by micro-cantilever tests, *Acta Mater.* 96 (2015) 249–257, doi:10.1016/j.actamat.2015.06.020.
- [28] A. Patra, D.L. McDowell, Continuum modeling of localized deformation in irradiated bcc materials, *J. Nucl. Mater.* 432 (2013) 414–427, doi:10.1016/j.jnucmat.2012.08.021.
- [29] A. Patra, D.L. McDowell, Crystal plasticity investigation of the microstructural factors influencing dislocation channeling in a model irradiated bcc material, *Acta Mater.* 110 (2016) 364–376, doi:10.1016/j.actamat.2016.03.041.
- [30] J. Nie, Y. Liu, P. Lin, Q. Xie, Z. Liu, A crystal plasticity model with irradiation effect for the mechanical behavior of FCC metals, *Acta Mech. Solida Sin.* 32 (2019) 675–687, doi:10.1007/s10338-019-00145-z.
- [31] M. Zaiser, P. Moretti, H. Chu, Stochastic crystal plasticity models with internal variables: application to slip channel formation in irradiated metals, *Adv. Eng. Mater.* 22 (2020) 1901208, doi:10.1002/adem.201901208.
- [32] N.R. Barton, A. Arsenlis, J. Marian, A polycrystal plasticity model of strain localization in irradiated iron, *J. Mech. Phys. Solids* 61 (2013) 341–351, doi:10.1016/j.jmps.2012.10.009.
- [33] L.R. Chen, X.Z. Xiao, L. Yu, H.J. Chu, H.L. Duan, Texture evolution and mechanical behaviour of irradiated face-centred cubic metals, *Proc. R. Soc. A Math. Phys. Eng. Sci.* 474 (2018) 20170604, doi:10.1098/rspa.2017.0604.
- [34] U.F. Kocks, Superposition of alloy hardening, strain hardening, and dynamic recovery, *Energy Technol. Rev.* (1980) 1661–1680 Pergamon Press (Int Ser on the Strength and Fract of Mater and Struct), doi:10.1016/b978-1-4832-8412-5.50250-2.
- [35] T.O. Erinosho, F.P.E. Dunne, Strain localization and failure in irradiated zircaloy with crystal plasticity, *Int. J. Plast.* 71 (2015) 170–194, doi:10.1016/j.ijplas.2015.05.008.
- [36] S. Das, H. Yu, E. Tarleton, F. Hofmann, Hardening and strain localisation in helium-ion-implanted tungsten, *Sci. Rep.* 9 (2019) 1–14, doi:10.1038/s41598-019-54753-3.
- [37] A.J. Cackett, C.D. Hardie, J.J.H. Lim, E. Tarleton, Spherical indentation of copper: crystal plasticity vs experiment, *Materialia* 7 (2019) 100368, doi:10.1016/j.mta.2019.100368.
- [38] S. Das, H. Yu, K. Mizohata, E. Tarleton, F. Hofmann, Modified deformation behaviour of self-ion irradiated tungsten: a combined nano-indentation, HR-EBS and crystal plasticity study, *Int. J. Plast.* 135 (2020) 102817, doi:10.1016/j.ijplas.2020.102817.
- [39] X. Xiao, D. Terentyev, L. Yu, D. Song, A. Bakaev, H. Duan, Modelling irradiation-induced softening in BCC iron by crystal plasticity approach, *J. Nucl. Mater.* 466 (2015) 312–315, doi:10.1016/j.jnucmat.2015.08.017.
- [40] P. Chakraborty, S.B. Biner, Y. Zhang, B.W. Spencer, Crystal plasticity model of reactor pressure vessel embrittlement in GRIZZLY, Idaho Falls, ID (United States), 2015. doi:10.2172/1244616.
- [41] K. Suganuma, H. Kayano, S. Yajima, Mechanical properties changes of Fe-Cr alloys by fast neutron irradiation, *J. Nucl. Mater.* 105 (1982) 23–35, doi:10.1016/0022-3115(82)90448-2.
- [42] D. Terentyev, L. Malerba, D.J. Bacon, Y. Osetsky, The effect of temperature and strain rate on the interaction between an edge dislocation and an interstitial dislocation loop in α -iron, *J. Phys. Condens. Matter* (2007) 456211 IOP Publishing, doi:10.1088/0953-8984/19/45/456211.
- [43] R. Quey, P.R. Dawson, F. Barbe, Large-scale 3D random polycrystals for the finite element method: generation, meshing and remeshing, *Comput. Methods Appl. Mech. Eng.* 200 (2011) 1729–1745, doi:10.1016/j.cma.2011.01.002.
- [44] Y. Liu, X. Zhang, Y. Zhu, P. Hu, C. Oskay, Dislocation density informed eigen-strain based reduced order homogenization modeling: verification and application on a titanium alloy structure subjected to cyclic loading, *Model. Simul. Mater. Sci. Eng.* 28 (2020) 025004, doi:10.1088/1361-651X/AB602E.
- [45] Zirconium - mechanical properties and material applications, (n.d.). <https://www.azom.com/article.aspx?ArticleID=7645> (accessed July 26, 2021).
- [46] R.E. Voskoboinikov, Y.N. Osetsky, D.J. Bacon, Statistics of primary damage creation in high-energy displacement cascades in copper and zirconium, *Nucl. Instrum. Methods Phys. Res. Sect. B Beam Interact. Mater. At.* 242 (2006) 68–70, doi:10.1016/j.nimb.2005.08.166.
- [47] F. Gao, D.J. Bacon, L.M. Howe, C.B. So, Temperature-dependence of defect creation and clustering by displacement cascades in α -zirconium, *J. Nucl. Mater.* 294 (2001) 288–298, doi:10.1016/S0022-3115(01)00483-4.
- [48] D.R. Mason, X. Yi, A.E. Sand, S.L. Dudarev, Experimental observation of the number of visible defects produced in individual primary damage cascades in irradiated tungsten, *EPL (Europhys. Lett.)* 122 (2018) 66001, doi:10.1209/0295-5075/122/66001.
- [49] A. Harte, D. Jädernäs, M. Topping, P. Frankel, C.P. Race, J. Romero, L. Hallstadius, E.C. Darby, M. Preuss, The effect of matrix chemistry on dislocation evolution in an irradiated Zr alloy, *Acta Mater.* 130 (2017) 69–82, doi:10.1016/j.actamat.2017.03.024.
- [50] R. Thomas, D. Lunt, Dataset for: the effect of loading direction on slip and twinning in an irradiated zirconium alloy, (2021). 10.5281/ZENODO.5566869.
- [51] M.D. Atkinson, R. Thomas, A. Harte, P. Crowther, J. Quinta da Fonseca, DeFDP: deformation data analysis in python - v0.92, (2020). doi:10.5281/ZENODO.3784775.

- [52] S. Naka, A. Lasalmonie, P. Costa, L.P. Kubin, The low-temperature plastic deformation of α -titanium and the core structure of a-type screw dislocations. 57 (2006) 717–740, doi:[10.1080/01418618808209916](https://doi.org/10.1080/01418618808209916).
- [53] A. Marano, L. Gélébart, S. Forest, Intragranular localization induced by softening crystal plasticity: analysis of slip and kink bands localization modes from high resolution FFT-simulations results, *Acta Mater.* 175 (2019) 262–275.
- [54] A. Marano, L. Gélébart, S. Forest, FFT-based simulations of slip and kink bands formation in 3D polycrystals: influence of strain gradient crystal plasticity, *J. Mech. Phys. Solids* 149 (2021) 104295, doi:[10.1016/j.jmps.2021.104295](https://doi.org/10.1016/j.jmps.2021.104295).
- [55] S. Das, F. Hofmann, E. Tarleton, Consistent determination of geometrically necessary dislocation density from simulations and experiments, *Int. J. Plast.* 109 (2018) 18–42, doi:[10.1016/j.ijplas.2018.05.001](https://doi.org/10.1016/j.ijplas.2018.05.001).